

# An investigation of a GJ 1214b-like exoplanet with a water vapor atmosphere using a simple general circulation model

Angela M. Zalucha<sup>a</sup>, Timothy I. Michaels<sup>b</sup>, Nikku Madhusudhan<sup>c</sup>

<sup>a</sup>*A. M. Zalucha Consulting, 1050 Walnut St., Boulder, Colorado, 80302, USA*

<sup>b</sup>*Southwest Research Institute, Department of Space Studies, 1050 Walnut St., Boulder, Colorado, 80302, USA*

<sup>c</sup>*Yale University, Department of Physics and Department of Astronomy, New Haven, Connecticut, 06511, USA*

Number of pages: 62

Number of tables: 1

Number of figures: 21

**Proposed Running Head:**

Simple GCM study of a GJ 1214b-like exoplanet

**Please send Editorial Correspondence to:**

Angela M. Zalucha

1050 Walnut Street

Suite 300

Boulder, CO 80302, USA

Email: [angela@boulder.swri.edu](mailto:angela@boulder.swri.edu)

Phone: (720) 208-7211

## ABSTRACT

We present results from a simple general circulation model (GCM) of a GJ 1214b-like super-Earth exoplanet. The dynamical core of our model is a scaled-up version of a shallow atmosphere, terrestrial planet GCM that has previously been used for Mars and therefore employs different boundary conditions and physical processes than downsized gas giant models. We assume the planet is tidally locked and has the observed characteristics of GJ-1214b [Charbonneau et al. 2009] for surface mass, surface radius, orbital period, and surface gravitational acceleration. We assume the atmosphere is composed entirely of water vapor. We assume the planet has a surface (i.e., a density discontinuity at depth), which will provide a mechanical drag and affect the radiative balance at the bottom boundary. We assume a gray atmosphere in the IR. We find that a westerly jet is present aloft at the equator and that the longitude of maximum temperature is shifted eastward of the substellar point. A wavenumber-1 feature is present in the equatorial vertical velocity field, indicative of a standing Kelvin and/or Rossby wave. As such, the circulation does not exhibit a cellular structure as on terrestrial Solar System planets; rather, air parcels move up and down on closed horizontal circuits and always return to the same location. The flow at the midlatitudes and poles has both an easterly component and a component that flows poleward along the evening terminator and equatorward along the morning terminator. Temperature inversions exist in the boundary layer and aloft, which are a result of variations in horizontal heat transport. The flow within

the boundary layer is more convergent than in the atmosphere aloft. The surface pressure is higher at the poles than the equator. We also find that, as expected from simple energy balance arguments, as global mean surface pressure (i.e., atmospheric mass) increases, the mean atmospheric temperature increases; as surface (geometric) albedo increases, the mean atmospheric temperature decreases. From a momentum standpoint, as surface pressure increases: 1) the speed of the equatorial jet decreases on the dayside, 2) the latitudinal extent of the equatorial jet increases on the nightside, 3) the speed of the midlatitude zonal component of flow increases on the nightside, and 4) the speed of the meridional component of flow increases. Additionally, as surface albedo increases 1) The zonal wind speed decreases, 2) the latitudinal width of the equatorial jet decreases, and 3) the meridional wind speed decreases.

*Keywords:* ATMOSPHERES, DYNAMICS ; EXTRASOLAR PLANETS ;  
ATMOSPHERES, STRUCTURE

## 1. Introduction

Infrared observations of transiting extrasolar planets over the past decade have opened a window on a new regime of atmospheric dynamics (e.g., Knutson et al., 2007; Showman et al., 2009). The first transiting exoplanets discovered and modeled were “hot Jupiters”, planets broadly similar in size to Jupiter that orbit their parent stars in close-in orbits (often with periods less than a few Earth-days) and hence receive an immense amount of stellar flux (Mayor and Queloz, 1995; Charbonneau et al., 2000). Their masses and radii suggest that their atmospheres are hydrogen-dominated (Fortney et al., 2007), similar to Solar System gas giants, as opposed to terrestrial-type planets with solid and/or liquid surfaces and shallow atmospheres. They are also expected to be tidally-locked, always keeping one face to their parent star. These properties imply that their circulation patterns will be entirely unlike anything found in the Solar System.

Showman et al. (2008) simulated the atmospheres of the hot Jupiters HD 209458b and HD 189733b using a 3-D general circulation model (GCM) that was radiatively forced using Newtonian relaxation to a radiative equilibrium state. Showman et al. (2009) continued this work using a radiative transfer (RT) scheme that calculated the RT fluxes directly. Both of these studies showed flow from the substellar to antistellar point along the equator and over the poles at lower pressures, while an eastward equatorial jet and westward polar flow developed at higher pressures. Lewis et al. (2010) used a GCM to study hot Neptunes and found that as atmospheric metal-

licity was increased the circulation changed from being dominated by mid-latitude jets and minimal longitudinal temperature differences to one dominated by an equatorial jet and large day-night temperature differences. Many other gas giant-type GCMs have been recently developed (Cho et al., 2008; Langton and Laughlin, 2008; Dobbs-Dixon and Lin, 2008; Menou and Rauscher, 2009).

Recent observational advancements are leading to discoveries of much smaller transiting planets than the canonical hot Jupiters and Neptunes, namely super-Earths (Charbonneau et al., 2009; Léger and et al., 2009; Batalha and et al., 2011). Super-Earths are loosely defined as planets with masses of 1–10 that of Earth, and radii of  $\sim 1$ –3 times that of Earth, depending on the bulk composition (Seager et al., 2007; Valencia et al., 2007). The atmospheres of super-Earths are significantly different in their underlying physical properties and require different modeling considerations. First, the radiative balance of the atmosphere is different from gas giants due to the presence of an abrupt bottom-located high-emissivity infrared radiation source and potentially boundary layer convection and small-scale turbulence. This type of RT boundary condition is different from gas giant type models that assume an internal temperature that represents the heat source due to release of gravitational potential energy from the planet’s collapse. In the terrestrial-type case, the bottom radiative heat source is not a free parameter, while in the gas giant-type case it is. Second, the presence of a density discontinuity below the atmosphere, such as a solid surface or liquid ocean, will create a

mechanical barrier and a drag force through surface friction. Even before the discovery of smaller exoplanets, Joshi et al. (1997) and Joshi (2003) examined the habitability of synchronously-rotating Earth-sized planets around M-dwarf stars. They found that near the ground a thermally-direct longitudinal cell transported heat from the dayside to the nightside, while aloft the zonal-mean winds exhibited superrotation.

With the discovery of the transiting super-Earth GJ 1214b (Charbonneau et al., 2009), several idealized studies of this type of planet have been performed. Miller-Ricci and Fortney (2010a) computed 1-D model transit spectra using radiative-equilibrium temperature profiles corresponding to the physical conditions of GJ 1214b. They tested different atmospheric compositions but were unable to constrain the model spectra using spectral data (Bean et al., 2010). Merlis and Schneider (2010) used a 3-D GCM to study a tidally-locked Earth-like planet with a semi-gray atmosphere (considering longwave CO<sub>2</sub>-like and H<sub>2</sub>O-like absorbers) at two different rotation periods: 1 Earth-day and 1 Earth-year. They found that in both cases, the heat transport to the nightside was efficient in mediating the day-night temperature contrast. In the quickly rotating case, the atmospheric circulation and temperature patterns were dominated by eddies and waves. In the slowly rotating case thermally-divergent flow was dominant. Menou (2012) used a mini-Neptune-type 3-D GCM to model GJ 1214b with various compositions (water, super-solar or solar metallicity) and optional magnetohydrodynamic (MHD) drag. Wordsworth et al. (2011) used a 3-D GCM to investigate the habitability of

another super-Earth, GJ 581d, although this planet has not been observed to transit. Heng and Vogt (2011) used a 3-D GCM to model another super-Earth, Gliese 581g.

Here we present simple GCM results for atmospheric circulation, surface pressure, and temperature of a GJ 1214b-like planet. Two approaches from different mathematical limits have emerged in modeling of super-Earth atmospheres. One is that they are a small gas-giant planet (or mini-Neptune), which has no density discontinuity (i.e., no solid or liquid surface) and has an internal heat flux. This procedure naturally evolved out of the fact that the first exoplanets to be discovered were more Jupiter-like. The other modeling technique is to assume that super-Earths are like large terrestrial bodies such as Earth, Mars, Venus, and Titan, with rocky surfaces and relatively shallow atmospheres, based on existing models of these bodies that have long been used in Solar System studies. We follow the latter approach here.

Recent spectral observations (Bean et al., 2010, 2011; Désert et al., 2011; Crossfield et al., 2011; Berta et al., 2012) indicate that the atmospheric composition is metal-rich (except Croll et al., 2011, who determine the opposite), but do not constrain the composition any further.  $\text{H}_2\text{O}$  and  $\text{CO}_2$  have been suggested as possible candidates. We assume an  $\text{H}_2\text{O}$  atmospheric composition and the bulk parameters of GJ 1214b from Charbonneau et al. (2009) as input parameters in our GCM. We investigate a range of global mean surface pressures ( $10^4$ – $10^7$  Pa) and surface albedos (0.1–0.7), since these are not yet constrained by observations. In Section 2 we describe the simple 3-D GCM



dynamical core (based on the Massachusetts Institute of Technology GCM) and RT parameterization. In Section 3 we present results and discussion, including a comparison between modeled and observed transmission spectra.

## **2. Simple general circulation model configuration**

### *2.1. Dynamical core*

The dynamical core of the Massachusetts Institute of Technology (MIT) GCM solves the fundamental equations of geophysical fluid dynamics in 3-D using a finite volume method on an Arakawa C-grid (Marshall et al., 1997) on a sphere. The model atmosphere is hydrostatic and compressible, and may exchange mass with the surface via a source/sink term in the continuity equation. Convective adjustment is performed on the temperature profiles to prevent superadiabatic temperature profiles. The default configuration has neither viscosity nor vertical diffusion, but uses an eighth-order Shapiro filter to remove purely numerical noise. In the horizontal a cubed-sphere grid (Adcroft et al., 2004) with  $32 \times 32$  points per cube face is used, equivalent to a grid spacing of  $2.8^\circ$  at the equator. Compared to the more common cylindrical projection grid (i.e., a latitude/longitude grid), this type of horizontal grid eliminates singularities at the poles that force meridional winds to zero and removes the requirement for Fourier filtering in the high latitudes (in order to maintain a practical timestep).

The vertical grid is an  $\eta$  coordinate (Adcroft et al., 2004) based in atmospheric pressure and is scaled according to the prescribed global mean surface

pressure.  $\eta$  coordinates have the advantage of being based in atmospheric pressure (which reduce the governing equations to a simpler form than height coordinates) and do not suffer large pressure gradient errors near the surface when the topography is non-zero (as with a terrain-following or  $\sigma$  coordinate). In general, surfaces of constant  $\eta$  will intersect the surface, making computation more difficult, though for our purposes we assume flat topography and this is not a concern. We assume that the gravitational acceleration is constant with height within the region of the atmosphere relevant to this work.

The horizontal momentum equation is given by:

$$\frac{\partial \mathbf{u}_h}{\partial t} = -f \hat{\mathbf{k}} \times \mathbf{u}_h - \nabla_h \Phi + \mathbf{F}_h, \quad (1)$$

where  $t$  is time,  $\mathbf{u}_h$  is the horizontal component of velocity,  $f = 2\Omega \sin \phi$  is the Coriolis parameter (where  $\Omega$  is the planetary rotation rate and  $\phi$  is latitude),  $\Phi$  is the geopotential height,  $\nabla_h$  indicates that only the horizontal component of the gradient should be considered, and  $\mathbf{F}_h$  is the frictional drag. Here friction arises from drag on the atmosphere by the surface, given by (following Held and Suarez, 1994)

$$\mathbf{F}_h = -k_f \max \left( 0, \frac{p - p_b}{p_s - p_b} \right) \mathbf{u}_h \quad (2)$$

where  $k_f$  is the wind damping rate,  $p$  is pressure,  $p_s$  is the surface pressure (a function of time and space), and  $p_b = 0.7p_s$  is the pressure at the top

altitude of the boundary layer, defined as the part of the atmosphere where the drag is nonzero. Eq. 2 represents a drag law (linearly dependent on the horizontal velocity) that decreases with height, reaches zero at the top of the boundary layer, and is zero at all levels above. It reflects the diminishing dynamical influence of the surface as the altitude is increased, and the fact that the boundary layer tends to follow the height of the surface terrain (i.e., the top of the boundary layer will generally be higher where the surface elevation is higher). Held and Suarez (1994), which is an idealized GCM for Earth, uses  $k_f = 1 \text{ day}^{-1}$ . Mars models use frictional time scales of 0.2 to 10 sols (Joshi et al., 1995), 1 sol (Lewis et al., 1996), 0.25-0.7 sol (Nayvelt et al., 1997), and  $\sim 20$  sols (Caballero et al., 2008). These relationships are determined empirically through modeling of near-surface atmospheric properties. We take them to be representative of terrestrial-like bodies and use  $k_f = 1 \text{ day}^{-1}$ .

Zalucha et al. (2010) adapted the MIT GCM to Mars and used it to analyze the effect of topography on the Martian Hadley cells. Zalucha and Gulbis (2012) adapted the MIT GCM to Pluto and compared the results to observed stellar occultation light curves. Thus, the MIT GCM has been successfully adapted to other planets beyond its already wide usage as an Earth atmosphere and ocean model.

We have recently adapted and configured the MIT GCM for application to the super-Earth GJ 1214b using the observed parameters of Charbonneau et al. (2009) and assuming a 100%  $\text{H}_2\text{O}$  atmosphere. We refer to this version of the

GCM as a simple GCM because it does not use a sophisticated RT scheme (see Section 2.2). Table 1 shows the simple GCM parameters. Orbital eccentricity is constrained to  $< 0.27$  by Charbonneau et al. (2009), but this is still quite a large range for planetary climate. For instance, the Mars eccentricity of 0.0934 is enough to produce substantial differences between seasons. We assume a circular orbit for simplicity. The obliquity of GJ 1214b is unconstrained. We assume zero obliquity, which by definition means the planet will be at perpetual equinox and have no seasons. The variation of super-Earth climate with non-zero obliquities is a subject of future work.

## 2.2. *RT scheme*

An important distinction exists between terrestrial-type models as described here and gas giant-type models (e.g., Showman et al., 2009). Terrestrial-type models have a solid or liquid surface at the bottom boundary of the model, which provides a source of friction. Moreover, they do not contain a significant internal heat source, which is a free parameter in giant planet-type models. In a terrestrial-type model surface fluxes and surface temperature are in balance with the atmospheric and incoming stellar flux and are not free parameters. Near-surface convection may also be present. Small-scale turbulence may induce momentum and heat transfer between the surface and atmosphere or within the lowest atmospheric layers. The surface may also have a large heat storage capacity like Earth’s oceans, which produce a large temperature lag in the seasons compared with the stellar zenith angle. We

assume an entirely rocky surface with a relatively low heat storage capacity.

Some mini-Neptune models (e.g., Miller-Ricci and Fortney, 2010a) use the Guillot (2010) RT scheme, which has a kink at mid-levels due to short-wave absorption. No terrestrial-type planets in our Solar System have observed vertical temperature structures like this, and a purely gray model at IR wavelengths is a better match to the lower atmospheres of Earth, Mars, Venus, and Titan. Intermediate models of scattering by solar absorption in terrestrial planet atmospheres have been previously developed (Toon et al., 1989; Briegleb, 1992), which may be incorporated into our model in the future.

In our simple GCM the planet is assumed to be tidally locked with its parent star (i.e., the same hemisphere of the planet is always illuminated by the star, while the opposite hemisphere remains perpetually in darkness). Like the Mars version of our simple GCM, we assume the diabatic heating term is given by

$$\frac{\partial T}{\partial t} = k_T(T - T_{eq}) \quad (3)$$

where  $T$  is the air temperature in the simple GCM,  $t$  is time,  $T_{eq}$  is the radiative equilibrium air temperature, and  $k_T$  is the radiative relaxation rate.  $k_T$  is a parameter that is calculated based on the  $e$ -folding time of a perturbation to the vertical temperature profile. For atmospheric radiative transfer in the Eddington approximation that is gray at long wavelengths and transparent at short wavelengths, the radiative transfer equation has the analytical

solution

$$\sigma T_{eq}^4 = (1 - A)Q_o(0.5 + 0.75\tau) \quad (4)$$

where  $\sigma$  is the Stefan-Boltzmann constant,  $A$  is the surface albedo,  $Q_o$  is the insolation (now including the diurnal variation), and  $\tau$  is the optical depth. The optical depth is linearly dependent on pressure as  $\tau = \tau_o(p/p_{oo})$ , where  $\tau_o$  is the optical depth at the reference pressure  $p_{oo}$  (in this case set equal to the surface pressure  $p_s$  since the topography is flat). Our gray atmosphere specification is equivalent to that derived by Guillot (2010) in the limit that the interior radiation term (i.e., infrared radiation emitted by the surface) dominates the shortwave stellar radiation directly absorbed by the atmosphere.  $\tau_o$  is the value from Merlis and Schneider (2010).

In the mathematical limit where the pressure in Eq. 4 approaches the surface pressure, there is a temperature discontinuity between the radiative equilibrium temperature of the surface and the radiative equilibrium temperature of the atmosphere just above the surface. To mitigate this unphysical property of the solution, convective adjustment is performed on Eq. 4 under the constraint of vertical flux balance. This procedure results in an equilibrium temperature that follows the adiabatic lapse rate in the lower atmosphere (the convective boundary layer) that is continuous with the equilibrium surface temperature and the upper atmosphere temperature given by Eq. 4. In addition, if the radiative equilibrium or simple GCM-predicted temperature drops below the condensation temperature, the temperature is

instantaneously reset to the condensation temperature (i.e., we do not explicitly consider any mass changes in the atmosphere) given by

$$T_{cond} = \left[ \frac{1}{T_1} - \frac{R}{L} \ln \left( \frac{p}{p_1} \right) \right]^{-1}, \quad (5)$$

where  $T_1$  the vaporization reference temperature,  $R$  is the specific gas constant,  $L$  is the specific latent heat of vaporization, and  $p_1$  is the vaporization reference pressure.

### 3. Simulation results and discussion

We performed simulations starting from rest, initializing with a globally constant temperature and surface pressure. After 120 Earth-days, the model reached a quasi-steady state, and the results were time averaged over the subsequent 400 days. This is a long time averaging period compared with Earth or Mars, but was necessary since long period ( $> 30$  day) oscillations were present in the modeled solution. In this paper, we are interested in the longer-term climate of a GJ 1214b-like planet, leaving such wave motions as an avenue of future work.

The globally averaged surface pressure, which is a representation of the atmosphere’s mass, is an important but unconstrained parameter for super-Earths. Since our atmosphere is assumed to be 100%  $\text{H}_2\text{O}$  vapor and consequently entirely made up of the radiatively active constituent, the global mean surface pressure is directly tied to the strength of the greenhouse ef-

fect. Higher global mean surface pressure means more IR absorption, and thus higher temperatures. We have chosen to perform simulations using the following global mean surface pressures:  $10^4$ ,  $10^5$ ,  $10^6$ , and  $10^7$  Pa. For reference, the global mean surface pressures of Venus, Earth, Mars, and Titan are approximately  $90 \times 10^5$  Pa,  $10^5$  Pa,  $0.006 \times 10^5$  Pa, and  $1.5 \times 10^5$  Pa, respectively.

The geometric albedo of a planet is also an important parameter for planetary atmospheres because it controls the amount of energy that is absorbed by the planet’s cross-section, and thus the amount of energy absorbed by the surface and re-emitted into the atmosphere. Albedo variations over the planet’s surface can be important depending on inhomogeneous surface compositions such as ocean, rock, ice, or clouds. We assume a constant surface albedo of 0.1, 0.4, and 0.7. Note that the globally averaged surface albedos of Venus, Earth, Mars, and Titan are approximately 0.77, 0.3, 0.15, and 0.22, respectively.

### *3.1. Results of the $10^5$ Pa surface pressure, 0.4 surface albedo case*

We examine in detail the results of the  $10^5$  Pa global mean surface pressure and 0.4 surface albedo case. This case is near the center of our parameter sweep and is the most similar to Earth.

Figure 1 shows temperature profiles from the equator and  $60^\circ$  latitude (midlatitude) at four local times. All of the temperature profiles contain a temperature inversion (temperature increasing with decreasing pressure)



near the surface, and the midlatitude profiles contain another inversion peaking at about  $10^3 Pa$ . The underlying radiative heating produces a radiative equilibrium (i.e., steady state with no wind) temperature that monotonically decreases with decreasing pressure (Eq. 4) because there are no shortwave absorbers and the optical depth decreases linearly with pressure. These inversions must be caused by dynamical heat transport, namely horizontal advection that is more efficient around the levels of the temperature inversions. Thus, dynamical heat transport has a non-negligible effect on atmospheric temperature.

Comparing pressure-temperature ( $p$ - $T$ ) profiles at the same local times indicates that at some altitudes the temperature is higher in the midlatitudes, which would not be expected through RT considerations alone because the stellar flux decreases as a function of latitude. The reversal occurs at pressures lower than  $\sim 10^3$  Pa and within a few  $10^4$  Pa of the surface. There is also a longitudinal asymmetry between the morning and evening terminators. At the equator, the evening temperature profile is greater than or equal to the morning temperature at all levels, while in the midlatitudes, the opposite is the case. Note that the temperature profiles are always greater than the condensation temperature of  $H_2O$ , because we have explicitly forbidden it in the model equations and parameterizations.

Figure 2 shows the wind structure of the free atmosphere (above the frictional boundary layer) at a pressure of 680 Pa. While quantitative differences exist at the levels outside the boundary layer (pressures less than

$0.7 \times 10^5$  Pa), they all exhibit a stationary wavenumber-1 longitudinal structure in the vertical velocity field. The circulation is divided into two latitudinal regimes. First, an equatorial region between  $\pm 30^\circ$  with a high speed ( $\geq 300 \text{ m s}^{-1}$ ) westerly jet<sup>1</sup>, sinking motion on the western (i.e., morning) hemisphere, and rising motion in the eastern (i.e., evening) hemisphere. Second, poleward of  $\pm 30^\circ$  where the flow is northward over the pole on the terminators and dayside and eastward around the nightside of the planet. Moreover, the sign of the vertical motions switch such that descent is on the evening hemisphere and ascent is on the morning hemisphere.

We do not see areas of strong divergence or convergence in the atmospheric circulation. Instead, air parcels travel on closed horizontal circuits around the planet while moving upwards and downwards, but always return to the same level after a complete horizontal cycle around the planet. To test this phenomenon, we performed a series of passive tracer experiments. The simple GCM was re-initialized from a fully spun-up state. Passive tracers, i.e., a concentration of radiatively inert substance subject only to advection and compression/expansion, were injected into the model at several latitude bins at 680 Pa and  $0^\circ$  longitude with a concentration of 10 units per gridpoint (concentration units or cu). The simple GCM was then time integrated in a normal fashion, and the concentration of the tracers at each time step was recorded. Figure 3 shows the 0.2 cu contour for the latitude bin from 0 to  $10^\circ$ .

---

<sup>1</sup>For reference, the sound speed in an ideal gas of water vapor is  $495 \text{ m s}^{-1}$  at 400 K and  $858 \text{ m s}^{-1}$  at 1200 K

The tracers are advected eastward, moving in a wave-like motion downwards and then upwards, finally returning to their initial starting point 76.8 hours later. Deformations in the shape of the tracer field are due to numerical conversion of the cube-sphere grid to a latitude-longitude grid and numerical errors in the advection scheme. At higher latitudes, the tracer also returns to the same starting point, but the 3D motion makes it difficult to show here.

Showman and Polvani (2011) derive analytic models for tidally locked, strongly irradiated, short-period exoplanets including both hot Jupiters and terrestrial-type planets. They show that the westerly, equatorial jet, which has the opposite sign on Earth, is maintained by standing equatorial Rossby and Kelvin waves. Indeed, our model results of a wavenumber-1 stationary wave pattern at the equator are consistent with this theory. Our results are most similar to their linear, analytic solution, except that the wind direction at the equator is everywhere westerly in our model. In the Showman and Polvani (2011) model, the winds are easterly in the equatorial western hemisphere. In this type of model (as described previously by Gill, 1980), easterly propagating Rossby waves are responsible for the easterly flow, and westerly propagating Kelvin waves are responsible for the westerly flow at the equator. The disagreement between our simple GCM and the Showman and Polvani (2011) model in this regard suggests that only Kelvin waves are present at the equator in our model.

The equatorial Rossby radius of deformation is given by

$$L_R = \left( \frac{\sqrt{gH}}{\beta} \right)^{1/2}, \quad (6)$$

where  $g$  is the gravitational acceleration at the surface,  $H$  is the shallow-water approximation depth (taken to be the depth of the model below the Rayleigh sponge layer,  $10^3$  km) and  $\beta = 2\Omega \cos \phi/a$ , where  $a$  is the planetary radius. Figure 4 shows the zonally-averaged zonal wind. In the Showman and Polvani (2011) model, the latitudinal extent of the equatorial jet is  $\pm L_R$ . In our simple GCM,  $L_R = 22^\circ$ , which is smaller than the jet width of  $\sim 30$ – $45^\circ$ .

Figure 5 shows the wind structure in the boundary layer at a pressure of 9377 Pa. The circulation has a different structure than in the free atmosphere. The midlatitudes are characterized by weak downwelling and a horizontal wavenumber-1 pattern. At the equator, an intense area of downwelling and easterly flow is present at the substellar point (12 hours LT), while there is an area of intense upwelling at 15 hours LT. Still farther to the east the upward motion switches back to downwelling.

### *3.2. Results of differing surface pressure and surface albedo*

The global mean surface pressure (i.e. the atmosphere’s total mass) and the surface albedo are not well constrained by observations; however, these are fundamental parameters that strongly modulate atmospheric processes. Figure 6 shows dayside, equatorial temperature profiles as a function of  $p_s$  and  $A$ . As  $p_s$  increases, temperature increases. This behavior occurs simply

because we have assumed that the atmosphere is entirely composed of the IR absorber ( $\text{H}_2\text{O}$ ), so as atmospheric mass increases, so does the amount of the absorber. The atmosphere subsequently absorbs more of the energy being reradiated by the surface. Similarly, temperature decreases as  $A$  increases because less of the incoming stellar flux is reflected to space.

### 3.2.1. *Free atmosphere*

Figure 7 shows simple GCM temperature in the free atmosphere (outside of the frictional boundary layer) as a function of  $p_s$  with  $A$  held constant. As  $p_s$  increases, the temperature increases at all locations, for reasons described above. In all cases, the equatorial temperature maximum is shifted eastward of the substellar point, as is also the case in hot Jupiter models (e.g., Showman et al., 2008). The maximum temperature exists offset from the equator at about  $30^\circ$  latitude and 12 hours LT. Thus, on the dayside as we move from equator to pole, the temperature first increases until this location is reached, then decreases towards the poles. In the midlatitudes, the temperature on a given latitude circle is maximum near 12 hours LT, but the exact longitude of the maximum is located on either side of this meridian depending on the direction of the zonal flow. A temperature minimum occurs at 0 hours LT and  $50^\circ$  latitude. On the nightside, the temperature decrease monotonically from equator to pole. These solutions again match the linear analytical model of Showman and Polvani (2011).

Figure 8, along with panel (b) of Fig. 7 (in the order Fig. 8a, Fig. 7b,

Fig. 8b), show the effect of increasing  $A$  on temperature in the free atmosphere ( $p_s$  held constant). Again, the effect on the horizontal structure is simply to decrease the temperature everywhere as  $A$  increases.

Figure 9 shows the zonal component of wind in the free atmosphere as a function of  $p_s$ . As  $p_s$  increases, the speed of the equatorial jet decreases between 9 and 15 hours LT. The latitudinal extent of the equatorial jet increases on the nightside. At the two greatest initial surface pressure cases ( $10^6$  and  $10^7$  Pa), an increasingly westerly component of flow develops at middle to high latitudes between 11 and 18 hours LT. The nightside, easterly flow in the midlatitudes also increases in speed as  $p_s$  increases. Figure 10, along with panel (b) of Fig. 9 (in the order Fig. 10a, Fig. 9b, Fig. 10b), show the effect of increasing surface albedo on zonal wind in the free atmosphere. The zonal wind speed in the equatorial and midlatitude jets decreases with increasing  $A$ . Also, the latitudinal width of the equatorial jet decreases as  $A$  increases.

Figures 11 and 12 show the effect of increasing  $p_s$  and  $A$ , respectively, on meridional flow in the same order as Figs. 9 and 10. All cases have areas of southerly flow at southern longitudes from 12–24 hours LT and northern longitudes from 0–12 hours LT and northerly flow elsewhere. In the cylindrical projection format of our plots, this behavior indicates that there is a component of the flow over the poles from the evening side (i.e., western hemisphere) to the morning side (i.e., eastern hemisphere). As  $p_s$  increases, the meridional wind speed increases; as  $A$  increases the speed decreases.

This behavior implies a link between the amount of thermal energy and the strength of winds.

### 3.2.2. *Boundary layer*

Figure 13 shows the time-integrated surface pressure as a function of latitude and longitude and  $p_s$ . Note the distinction between the global mean surface pressure ( $p_s$ ) and the latitudinally and longitudinally varying surface pressure—the latter is equal to  $p_s$  in the global sum. To show each case on the same scale, the latitudinally and longitudinally varying surface pressure has been normalized by  $p_s$  for that case, so what is actually shown is the surface pressure anomaly. The surface pressure is higher at the poles than at the equator, which is opposite of terrestrial-type Solar System bodies (Earth, Mars, Venus, and Titan). As  $p_s$  increases, the fractional difference between pole and equator decreases. In the  $p_s = 10^4$  and  $10^5$  Pa cases, the surface pressure variation is more longitudinally symmetric, with an entirely positive anomaly poleward of  $\sim 40 - 60^\circ$  and an entirely negative anomaly equatorward of this latitude circle. In the  $p_s = 10^6$  and  $10^7$  Pa cases, the surface pressure variation is entirely positive poleward of this latitude circle, but equatorward there are both positive and negative anomalies for a given latitude circle. The minimum surface pressure anomaly moves poleward and westward as  $p_s$  is increased; the maximum surface pressure anomaly moves mainly equatorward.

Figure 14, along with panel (b) of Fig. 13 (in the order Fig. 14a, Fig. 13b,

Fig. 14b), show the effect of increasing surface albedo on latitudinally and longitudinally varying surface pressure. The minimum negative anomaly strengthens and moves poleward and westward, but otherwise the effect of changing surface albedo is small on the surface pressure field.

Figure 15 shows temperature in the boundary layer as a function of  $p_s$  with  $A$  held constant. Again, temperature increases as  $p_s$  increases. The temperature maximum is located on the equator and at the substellar point (12 hours LT), although the contours are elongated in the eastward direction. The temperature minimum is also located on the equator at 0 hours LT, except in the  $p_s = 10^7$  Pa case where it is at  $\sim 40^\circ$  latitude. Figure 16, along with panel (b) of Fig. 15 (in the order Fig. 16a, Fig. 15b, Fig. 16b), show the effect of increasing  $A$  on temperature in the boundary layer ( $p_s$  held constant). As before, temperature increases as  $A$  decreases.

Figures 17 and 18 show the zonal component of wind in the boundary layer as a function of  $p_s$  and  $A$ . A localized area of westerly wind exists between about 3 and 15 hours LT and  $40^\circ$  latitude. The maximum speed in this area decreases with increasing  $p_s$  and  $A$ . Poleward of  $40^\circ$  latitude there is an easterly jet that is most prominent in the low  $p_s$  and  $A$  cases. As both  $p_s$  and  $A$  increase, the jet strength decreases and the maximum speed shifts locations to the equator at 18 hours LT.

Figures 19 and 20 show the meridional component of wind in the boundary layer as a function of  $p_s$  and  $A$ . The meridional wind field is complicated, but is generally a mirror image of itself reflected across the equator. A clear



trend does not exist as  $p_s$  and  $A$  are increased, except that in the  $p_s = 10^7$  case there is an abrupt amplification of wind speeds.

### 3.3. *Transmission spectra*

We compute model atmospheric spectra of GJ 1214b in order to compare with observations. Several groups in the recent past have reported observations of transmission spectra of GJ 1214b (Bean et al., 2010, 2011; Berta et al., 2012; Croll et al., 2011; Désert et al., 2011; de Mooij et al., 2012). The observations have revealed a degeneracy in the atmospheric composition, allowing for either an atmosphere with a high mean molecular weight (such as an  $\text{H}_2\text{O}$  or  $\text{CO}_2$  dominated atmosphere) or an atmosphere covered with a high-altitude haze or cloud layer (Miller-Ricci and Fortney, 2010b; Howe and Burrows, 2012; Benneke and Seager, 2012). In the present study, we considered the former possibility by modeling a  $\text{H}_2\text{O}$  dominated atmosphere. We compute transmission spectra from the simple GCM output using a line-by-line RT code adapted from Madhusudhan and Seager (2009). Given the  $p$ - $T$  profiles at the limb of the atmosphere and the assumed composition, our spectral model computes a transmission spectrum of planet under the assumption of hydrostatic equilibrium. Figure 21 shows our model spectra along with several observations from the literature. We show a model spectrum for our base case of an  $\text{H}_2\text{O}$  dominated atmosphere ( $10^5$  Pa global mean surface pressure and 0.4 surface albedo), along with spectra of  $\text{H}_2$  dominated atmosphere models for comparison. In agreement with previous

studies, we find that our model spectrum for an H<sub>2</sub>O dominated atmosphere is consistent with all the observations in the 0.8  $\mu\text{m}$  - 5  $\mu\text{m}$  range. On the other hand, the observations are inconsistent with spectra of H<sub>2</sub>-rich models.

### 3.4. Comparison with previous exoplanet GCMs

Several GCMs have been developed for a wide variety of exoplanets. Due to the fact that many exoplanets have been discovered and that there is no “standard” type of exoplanet, differences between GCMs are not only due to differences in the numerical specifications of models, but also the physical properties that each author has tried to represent.

Menou (2012) have recently created a model for GJ-1214b assuming an H<sub>2</sub>O atmosphere (among others); however their model does not have a solid surface like ours does, making it more like a Neptune-type planet. They assume a surface pressure of 10 bar ( $10^6$  Pa). They use the Guillot (2010) RT scheme, which includes an additional shortwave absorption term compared with our RT scheme. Thus their temperature profiles do not have the boundary layer or upper level inversion as our simple GCM results do, but do contain an isothermal layer (except at the pole) at pressures higher than 1 bar ( $10^5$  Pa). They also include the effect of MHD bottom drag. This is a unique concept to exoplanet modeling, whereby currents due to electrical charge in the lowest layers of the atmosphere create a mechanical resistance that is an additional source of momentum drag. While their zonally averaged zonal winds show a westerly equatorial jet as our model and other models

do, elsewhere the winds are weakly westerly. In our model, easterly winds lie in the midlatitudes and poles, thus being in better agreement with the Showman and Polvani (2011) linear analytical model.

Long before the discovery of super-Earth exoplanets, Joshi et al. (1997) used a terrestrial planet GCM, previously used for terrestrial Solar System planets, to simulate a tidally-locked exoplanet. They assumed a gray IR RT scheme similar to ours (representing a gas with  $\text{CO}_2$  or  $\text{H}_2\text{O}$  radiative properties). The model is somewhat of a blend of terrestrial (radius, gravity, gas constant, and stellar insolation) and Mars constants (for instance, the atmosphere can freeze and sublime according to  $\text{CO}_2$  parameters), but also has a slow, Titan-like rotation rate (16 Earth-days). Their results contain a longitudinal, thermally direct cell, which transports heat from the dayside to the nightside. The mass is returned to the dayside through the polar regions at low levels. Our model results do not contain any type of thermally direct cells (e.g., a Hadley or Walker cell), but instead follow a horizontal standing wave around the equator. In the Joshi et al. (1997) model, the circulation aloft is fairly longitudinally symmetric, and a superrotating jet is present at the equator. The winds are westerly almost everywhere, unlike our model and the linear analytic model of Showman and Polvani (2011) that contain midlatitude easterly jets.

Joshi (2003) followed up the work of Joshi et al. (1997) by adding more model features such as precipitation, clouds, and non-gray RT, in addition to increasing the grid resolution. The primary focus of that paper was the

hydrologic cycle and the effect of the distribution of continents on temperature. Convection leads to the presence of clouds that change the radiative balance and temperature in the atmosphere. Clouds are an avenue of future work in our model.

Merlis and Schneider (2010) used an idealized terrestrial-type GCM with a different gray RT scheme that prescribed an optical depth with one term linearly dependent on pressure (to represent  $\text{CO}_2$ ) and the other term as quartic in pressure (to represent  $\text{H}_2\text{O}$ ). They also included a hydrologic cycle. They considered two cases, one where the rotation period was equal to one Earth-year and the other where the rotation period was one Earth-day (both cases with a tidally-locked planet). They find that the quickly rotating case is dominated by stationary Rossby and Kelvin waves, but their wind (particularly, the lack of jet structure in the zonal wind component) and temperature fields do not have the same spatial distribution as our results.

Heng and Vogt (2011) used an Earth GCM with Held and Suarez (1994) radiative forcing (an idealized benchmark case often used in terrestrial simulations) to simulate another super-Earth, Gliese 581g, except for those parameters which are known from observation such as radius, surface gravitational acceleration, and rotation rate. They also perform a study of the variation of GCM results on surface pressure (they use  $1 \times 10^4$ ,  $1 \times 10^5$ ,  $3 \times 10^5$ ,  $1 \times 10^6$  Pa), but find no quantitative differences in the zonally averaged zonal wind profiles. This is contrary to our findings. Note that they are missing the midlatitude easterly winds that are present in our model. Their surface

meridional wind fields show more organized structure than ours. The surface temperature contours are not as elongated in the meridional direction as ours.

Wordsworth et al. (2011) simulated a different super-Earth, Gleise 581d to determine if a CO<sub>2</sub> atmosphere was stable against atmospheric collapse. Their surface temperature results for a tidally-locked (1:1 resonance) planet depend primarily on stellar zenith angle and have a permanent dayside and nightside. As the resonance is changed (1:2 and 1:10), the temperature becomes more zonally elongated. Their 1:1 resonance case is more strongly polarized with a dayside and nightside, whereas our boundary layer temperatures (Figs. 15 and 16) are more elongated in the meridional direction and the temperature maximum is shifted eastward.

Despite the large discrepancies that could occur between shallow, terrestrial planet-type atmospheres and deep, gas-giant type atmospheres, our model results are qualitatively similar to the results of Showman et al. (2008) and Showman et al. (2009) for HD 189733b. Both of these models and our model (in the free atmosphere) have the same westerly equatorial jet and easterly midlatitude jets, meridional flow over the poles, and temperature maximum eastward of the substellar point. We do use the same dynamical core as these authors; however different RT schemes and bottom boundary conditions should lead to significant differences.

## 4. Conclusions

We have simulated the general circulation of a super-Earth exoplanet, with physical characteristics similar to GJ-1214b, using the terrestrial planet dynamical core of the MIT GCM and a simple, gray RT code. We have assumed a tidally-locked, close-in planet with an entirely water vapor atmosphere. We have found that our model results are in good agreement with analytic theory (Showman and Polvani, 2011) by confirming the presence of a westerly jet aloft at the equator and the longitude of maximum temperature shifted eastward of the substellar point. The flow at the midlatitudes and poles has both an easterly component and a component that flows poleward on the evening terminator and equatorward on the morning terminator. The flow moves in closed horizontal circuits around the planet with vertical wave perturbations of wavenumber-1. The flow in the boundary layer has more structure and converges east of the substellar point. The surface pressure increases from equator to pole, which is the reverse of Solar System terrestrial-type planets.

We have focused on the effect of changing global mean surface pressure (i.e., atmospheric mass) and surface geometric albedo. As expected, these have the broad effect of increasing the temperature when global mean surface pressure is increased (due to a stronger greenhouse effect) and decreasing the temperature when surface albedo is increased (due to reflection of more incoming stellar energy). Changing these parameters also has noticeable effects on the flow speed and latitudinal width of jets. Changing the behavior of

the flow changes the advection of heat in the model, and in turn the temperature profile as a function of latitude and longitude. This would change the outgoing flux and is what would be detectable by observations.

The greatest room for improvement in our model would be to move to a non-gray RT scheme. While non-gray atmospheres are certainly within the realm of current modeling techniques, it does generally require better assumptions about the atmospheric composition. For instance, GCM dynamical cores are easily adapted to each Solar System terrestrial planet, but each requires a relatively specialized RT scheme due to the widely different temperature, pressure, and dominant radiative constituents. These are not well constrained for super-Earth exoplanets. Clouds are also an important atmospheric phenomenon due to their scattering and absorption properties. These would also be important additions to our model.

Our GCM has a relatively simple, linear boundary layer drag scheme and upper atmospheric drag scheme. These are more difficult to predict from first principles, however. Boundary layer physics on Earth is accomplished by *in situ* surface observations and then empirically modeled, and even for Mars is not well understood. In the upper atmosphere drag may be produced by breaking waves or radiative damping of waves, but due to their small scale nature are also difficult to observe in the Solar System. Advanced Solar System models also contain multi-layer subsurface models to take into account thermal conduction, but again this would be difficult to constrain remotely.

The mechanism for mass exchange between the surface and atmosphere (i.e., due to evaporation and condensation) is already present in our model from its importance in the Mars and Pluto atmosphere-surface systems. Its relevance for hot super-Earths is diminished since the atmosphere is efficient at transporting heat to the nightside and the temperature does not reach condensation thresholds there.

We have implicitly assumed a rocky surface, though there is no reason to believe that a surface ocean is not present, perhaps even with continents. If the ocean is made of water, it would have a high heat capacity and would be quite important to the atmosphere radiatively, as is demonstrated by Earth’s atmospheric-ocean coupling.

A great number of exoplanet GCMs have been developed to date. Different numerical techniques exist for modeling geophysical fluids (e.g., spectral models, latitude/longitude grids, cube-sphere grids). Moreover, each developer has differed in which additional processes they have included in the model (the RT scheme, precipitation, drag forces). The Earth atmosphere modeling community realized some time ago that some standardization was needed to verify that models were numerically consistent with each other and that it was not merely the choice of numerical technique. Intercomparison studies were performed where each model was run with the same basic configuration (such as same season, same length of time, and same radiative heating) and with most of the complex processes turned off. This type of study would be useful in the exoplanet modeling community to check for



self-consistency.

## References

- Adcroft, A., Campin, J.-M., Hill, C., Marshall, J., 2004. Implementation of an atmosphere-ocean general circulation model on the expanded spherical cube. *Mon. Wea. Rev.* 132, 2845–2863.
- Batalha, N. M., et al., 2011. Kepler’s first rocky planet: Kepler-10b. *Astrophys. J.* 729, 27.
- Bean, J. L., Désert, J.-M., Kabath, P., Stalder, B., Seager, S., Miller-Ricci Kempton, E., Berta, Z. K., Homeier, D., Walsh, S., Seifahrt, A., 2011. The optical and near-infrared transmission spectrum of the super-Earth GJ 1214b: Further evidence for a metal-rich atmosphere. *Astrophys. J.* 743, 92.
- Bean, J. L., Miller-Ricci Kempton, E., Homeier, D., 2010. A ground-based transmission spectrum of the super-Earth exoplanet GJ 1214b. *Nature* 468, 669–672.
- Benneke, B., Seager, S., 2012. Atmospheric retrieval for super-Earth atmospheres: Uniquely constraining the atmospheric composition with transmission spectroscopy. *apj*, submitted.
- Berta, Z. K., Charbonneau, D., Désert, J.-M., Miller-Ricci Kempton, E., McCullough, P. R., Burke, C. J., Fortney, J. J., Irwin, J., Nutzman, P.,

- Homeier, D., 2012. The flat transmission spectrum of the super-Earth GJ1214b from Wide Field Camera 3 on the Hubble Space Telescope. *Astrophys. J.* 747, 35.
- Briegleb, B. P., 1992. Delta-Eddington approximation for solar radiation in the NCAR community climate model. *J. Geophys. Res.* 97, 7603–7612.
- Caballero, R., Pierrehumbert, R. T., Mitchell, J. L., 2008. Axisymmetric, nearly inviscid circulations in non-condensing radiative-convective atmospheres. *Quart. J. Roy. Meteor. Soc.* 134, 1269–1285.
- Charbonneau, D., Berta, Z. K., Irwin, J., Burke, C. J., Nutzman, P., Buchhave, L. A., Lovis, C., Bonfils, X., Latham, D. W., Udry, S., Murray-Clay, R. A., Holman, M. J., Falco, E. E., Winn, J. N., Queloz, D., Pepe, F., Mayor, M., Delfosse, X., Forveille, T., 2009. A super-Earth transiting a nearby low-mass star. *Nature* 462, 891–894.
- Charbonneau, D., Brown, T. M., Latham, D. W., Mayor, M., 2000. Detection of planetary transits across a sun-like star. *Astrophys. J.* 529, L45–L48.
- Cho, J. Y.-K., Menou, K., Hansen, B. M. S., Seager, S., 2008. Atmospheric circulation of close-in extrasolar giant planets. i. global, barotropic, adiabatic simulations. *Astrophys. J.* 675, 817–845.
- Croll, B., Albert, L., Jayawardhana, R., Miller-Ricci Kempton, E., Fortney, J. J., Murray, N., Neilson, H., 2011. Broadband transmission spectroscopy

- of the super-Earth GJ 1214b suggests a low mean molecular weight atmosphere. *Astrophys. J.* 736, 78.
- Crossfield, I. J. M., Barman, T., Hansen, B. M. S., 2011. High-resolution, differential, near-infrared transmission spectroscopy of GJ 1214b. *Astrophys. J.* 736, 132.
- de Mooij, E. J. W., Brogi, M., de Kok, R. J., Koppenhoefer, J., Nefs, S. V., Snellen, I. A. G., Greiner, J., Hanse, J., Heinsbroek, R. C., Lee, C. H., van der Werf, P. P., 2012. Optical to near-infrared transit observations of super-Earth GJ 1214b: water-world or mini-Neptune? *Astron. Astrophys.* 538, A46.
- Désert, J.-M., Bean, J., Miller-Ricci Kempton, E., Berta, Z. K., Charbonneau, D., Irwin, J., Fortney, J., Burke, C. J., Nutzman, P., 2011. Observational evidence for a metal-rich atmosphere on the super-Earth GJ1214b. *Astrophys. J.* 731, L40.
- Dobbs-Dixon, I., Lin, D. N. C., 2008. Atmospheric dynamics of short-period extrasolar gas giant planets. i. dependence of nightside temperature on opacity. *Astrophys. J.* 673, 513–525.
- Fortney, J. J., Marley, M. S., Barnes, J. W., 2007. Planetary radii across five orders of magnitude in mass and stellar insolation: Application to transits. *Astrophys. J.* 659, 1661–1672.

- Gill, A. E., 1980. Some simple solutions for heat-induced tropical circulation. *Quart. J. Roy. Meteor. Soc.* 106, 447–462.
- Guillot, T., 2010. On the radiative equilibrium of irradiated planetary atmosphere. *Astron. Astrophys.* 520.
- Held, I. M., Suarez, M. J., 1994. A proposal for the intercomparison of the dynamical cores of atmospheric general circulation models. *Bull. Amer. Meteor. Soc.* 75 (10), 1825–1830.
- Heng, K., Vogt, S. S., 2011. Gliese 581g as a scaled-up version of earth: atmospheric circulation simulations. *Montly Notices of the Royal Astronomical Society* 415, 2145–2157.
- Howe, A. R., Burrows, A. S., 2012. Theoretical transit spectra for GJ 1214b and other "Super-Earths". *Astrophys. J.*, submitted.
- Joshi, M., 2003. Climate model studies of synchronously rotating planets. *Astrobiology* 3, 415–427.
- Joshi, M. M., Haberle, R. M., Reynolds, R. T., 1997. Simulations of the atmospheres of synchronously rotating terrestrial planets orbiting M dwarfs: Conditions for atmospheric collapse and the implications for habitability. *Icarus* 129, 450–465.
- Joshi, M. M., Lewis, S. R., Read, P. L., Catling, D. C., 1995. Western boundary currents in the Martian atmosphere: Numerical simulations and observational evidence. *J. Geophys. Res.* 100 (E3), 5485–5500.

- Knutson, H. A., Charbonneau, D., Allen, L. E., Fortney, J. J., Agol, E., Cowan, N. B., Showman, A. P., Cooper, C. S., Megeath, S. T., 2007. A map of the day-night contrast of the extrasolar planet HD 189733b. *Nature* 447, 183–186.
- Langton, J., Laughlin, G., 2008. Hydrodynamic simulations of unevenly irradiated Jovian planets. *Astrophys. J.* 674, 1106–1116.
- Léger, et al., 2009. Transiting exoplanets from the CoRoT space mission. VIII. CoRoT-7b: the first super-Earth with measured radius. *Astron. Astrophys.* 506, 287–302.
- Lewis, N. K., Showman, A. P., Fortney, J. J., Marley, M. S., Freedman, R. S., Lodders, K., 2010. Atmospheric circulation of eccentric hot Neptune GJ436b. *Astrophys. J.* 720, 344–356.
- Lewis, S. R., Read, P. L., Collins, M., 1996. Martian atmospheric data assimilation with a simplified general circulation model: orbiter and lander networks. *Planet. Space Sci.* 44 (11), 1395–1409.
- Madhusudhan, N., Seager, S., 2009. A temperature and abundance retrieval method for exoplanet atmospheres. *Astrophys. J.* 707, 24–39.
- Marshall, J., Adcroft, A., Hill, C., Perelman, L., Heisey, C., 1997. A finite-volume, incompressible Navier Stokes model for studies of the ocean on parallel computers. *J. Geophys. Res.* 102, 5753–5766.

- Mayor, M., Queloz, D., 1995. A Jupiter-mass companion to a solar-type star. *Nature* 378, 355–359.
- Menou, K., 2012. Atmospheric circulation and composition of GJ1214b. *Astrophys. J.* 744, L16.
- Menou, K., Rauscher, E., 2009. Atmospheric circulation of hot Jupiters: a shallow three-dimensional model. *Astrophys. J.* 700, 887–897.
- Merlis, T. M., Schneider, T., 2010. Atmospheric dynamics of Earth-like tidally locked aquaplanets. *Journal of Advances in Modeling Earth Systems* 2, 1–17.
- Miller-Ricci, E., Fortney, J. J., 2010a. The nature of the atmosphere of the transiting super-Earth GJ 1214b. *Astrophys. J.* 716, L74–L79.
- Miller-Ricci, E., Fortney, J. J., 2010b. The nature of the atmosphere of the transiting super-Earth GJ 1214b. *Astrophys. J.* 716, L74–L79.
- Nayvelt, L., Gierash, P. J., Cook, K. H., 1997. Modeling and observations of Martian stationary waves. *J. Atmos. Sci.* 54, 986–1013.
- Seager, S., Kuchner, M., Hier-Majumder, C. A., Militzer, B., 2007. Mass-radius relationships for solid exoplanets. *Astrophys. J.* 669, 1279–1297.
- Showman, A. P., Cooper, C. S., Fortney, J. J., Marley, M. S., 2008. Atmospheric circulation of hot Jupiters: Three-dimensional circulation models

- of HD 209458b and HD 189733b with simplified forcing. *Astrophys. J.* 682, 559–576.
- Showman, A. P., Fortney, J. J., Lian, Y., Marley, M. S., Freedman, R. S., Knutson, H. A., Charbonneau, D., 2009. Atmospheric circulation of hot Jupiters: Coupled radiative-dynamical general circulation model simulations of HD 189733b and HD 209458b. *Astrophys. J.* 699, 564–584.
- Showman, A. P., Polvani, L. M., 2011. Equatorial Superrotation on Tidally Locked Exoplanets. *Astrophys. J.* 738, 71.
- Toon, O. B., McKay, C. P., Ackerman, T. P., Santhanam, K., 1989. Rapid calculation of radiative heating rates and photodissociation rates in inhomogeneous multiple scattering atmospheres. *J. Geophys. Res.* 94, 16287–16301.
- Valencia, D., Sasselov, D. D., O’Connell, R. J., 2007. Detailed models of super-Earths: how well can we infer bulk properties? *Astrophys. J.* 665, 1413–1420.
- Wordsworth, R. D., Forget, F., Selsis, F., Millour, E., Charnay, B., Madeleine, J.-B., 2011. Gliese 581d is the first discovered terrestrial-mass exoplanet in the habitable zone. *Astrophys. J.* 733, L48.
- Zalucha, A. M., Gulbis, A. A. S., 2012. Comparison of a simple 2D Pluto general circulation model with stellar occultation light curves and implications for atmospheric circulation. *Icarus* submitted.

Zalucha, A. M., Plumb, R. A., Wilson, R. J., 2010. An analysis of the effect of topography on the Martian Hadley cells. *J. Atmos. Sci.* 67, 673–693.



Table 1: Selected parameters simple GCM parameters: all simulations

Parameter	Value
Surface gravitational acceleration, $g$	$8.93 \text{ m s}^{-1}$
Orbital eccentricity	0
Orbital semimajor axis	$2.1426 \times 10^9 \text{ m}$
Stellar mass	$3.1243 \times 10^{29} \text{ kg}$
Rotation rate ( $\Omega$ )	$4.602 \times 10^{-5} \text{ s}^{-1}$
Obliquity	$0^\circ$
Solar constant	$21519 \text{ W m}^{-2}$
Surface emissivity, $\epsilon$	1.0
Radius	17059 km
Friction time scale ( $1/k_f$ )	1 Earth-day
Specific heat at constant pressure	$1850 \text{ J kg}^{-1} \text{ K}^{-1}$
Specific latent heat of vaporization	$22.6 \times 10^5 \text{ J kg}^{-1}$
Vaporization reference pressure	$1.01325 \times 10^5 \text{ Pa}$
Vaporization reference temperature	373 K
Specific gas constant	$461 \text{ J kg}^{-1} \text{ K}^{-1}$
Ratio of specific gas constant to specific heat	1/4
Longwave column optical depth at $10^5 \text{ Pa}$ ( $\tau_o$ )	$1.2 \times 10^5 \text{ Pa}$
Radiative relaxation time scale ( $1/k_T$ )	12.6 Earth-days

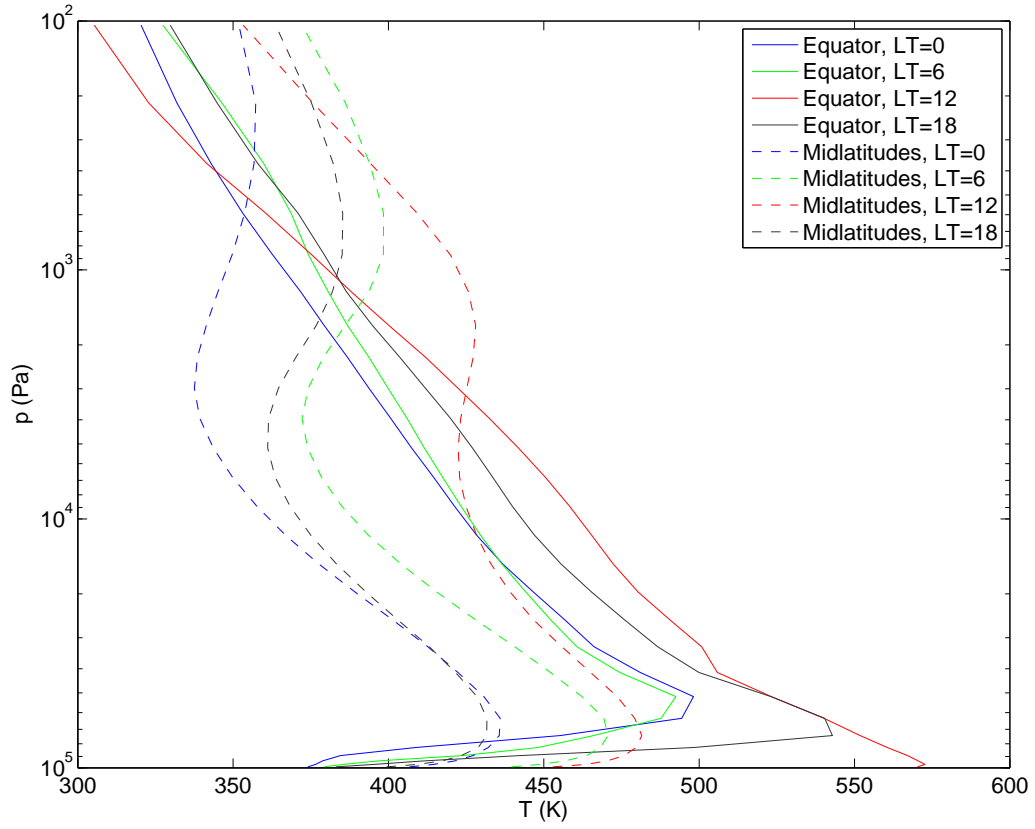


Figure 1: Temperature profiles from simple GCM (global mean surface pressure= $10^5$  Pa, surface albedo=0.4 case). The profiles are time averaged over 400 Earth-days. Two latitudes are shown: the equator and  $60^\circ$ (midlatitudes). Local times (LT) are plotted for the nightside (0 LT), dayside (12 LT), and morning (6 LT) and evening (18 LT) terminators.

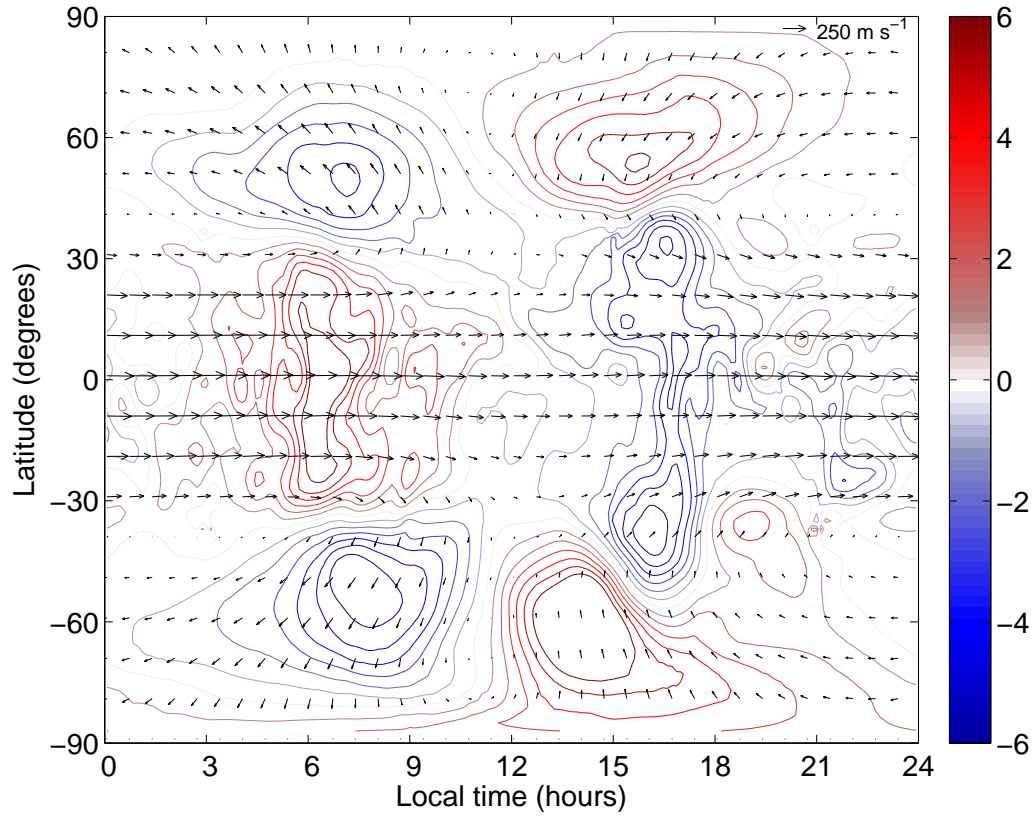


Figure 2: Horizontal winds (arrows, in  $\text{m s}^{-1}$ ) and vertical winds in pressure coordinates (colored contours, in  $10^{-2} \text{ Pa s}$ ) from simple GCM with global mean surface pressure= $10^5 \text{ Pa}$  and surface albedo=0.4 case. Time averaging was performed over 400 Earth-days. The winds are shown as an example of the circulation in the free atmosphere at 680 Pa. Note that in pressure coordinates positive vertical wind is downward.

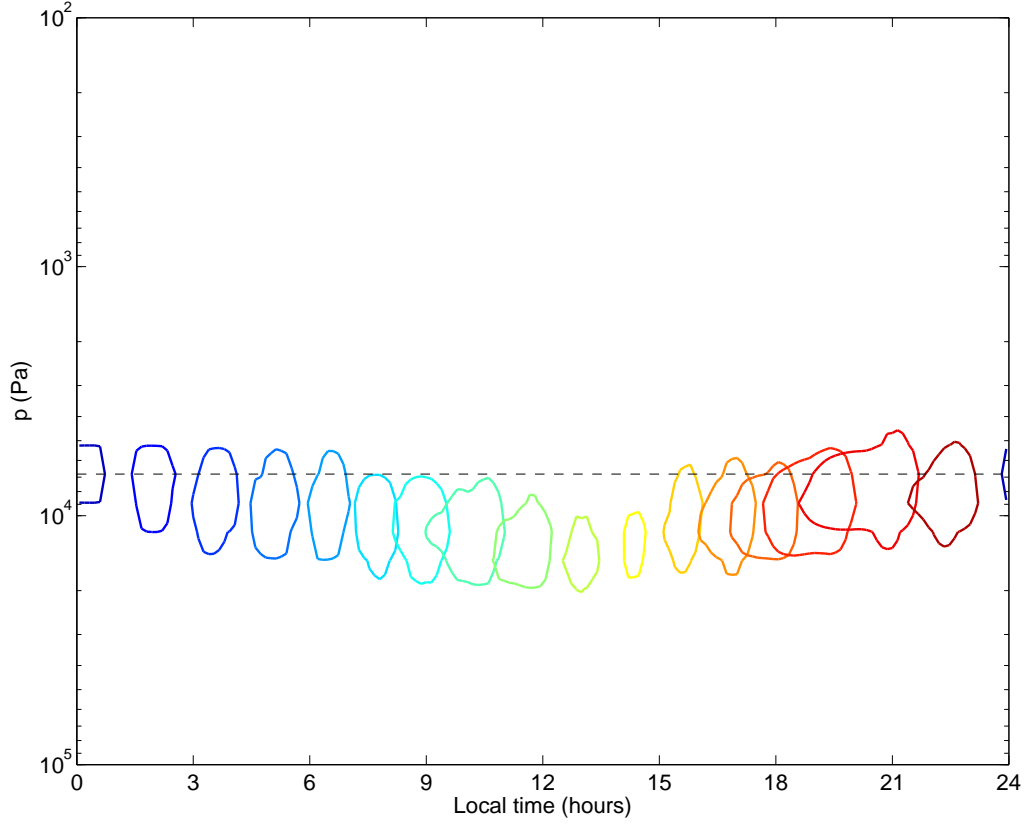


Figure 3: Passive tracer experiment (global mean surface pressure= $10^5$  Pa and surface albedo=0.4 case). Tracers were initialized between 0 and  $10^\circ$  latitude centered at  $0^\circ$  longitude and 680 Pa, corresponding to the darkest blue area. The closed curves are the 0.2 concentration contour. The area of tracers moves eastward, and the progression of time is indicated by changing hue (blue, cyan, green, yellow, orange, red) and replotted every 4.8 hours. The area of tracers remains in the longitude-height plane and returns to its initial starting position 76.8 hours later.

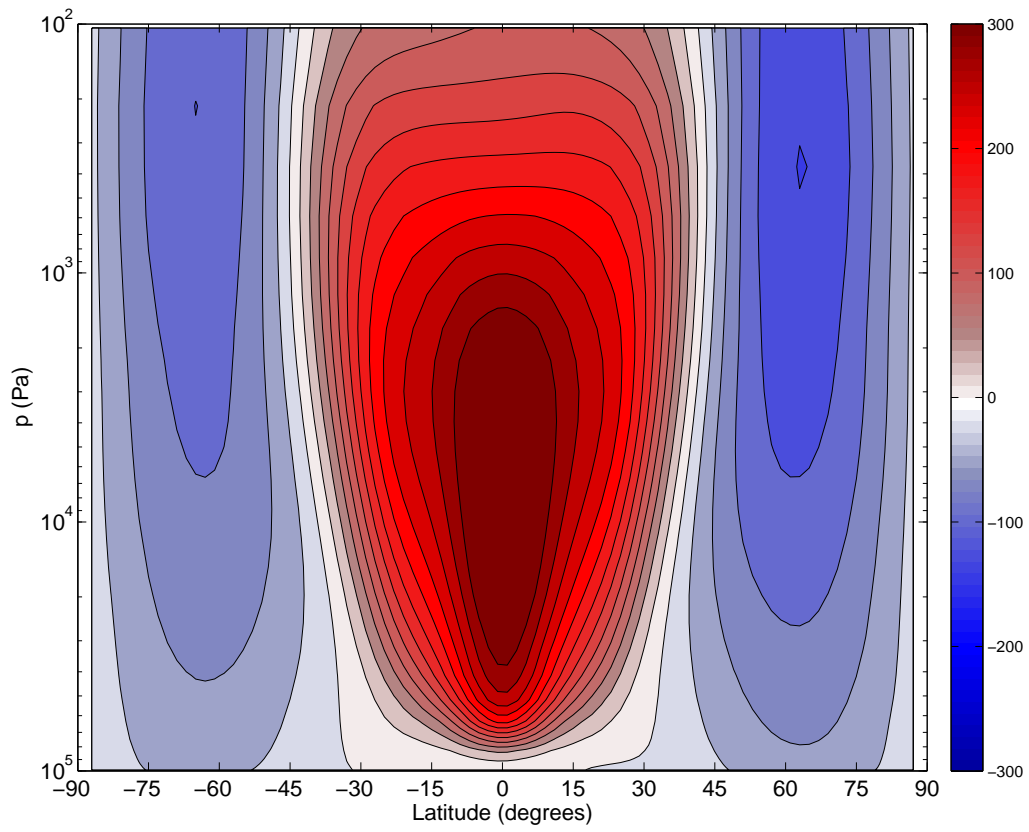


Figure 4: Zonally averaged zonal winds from simple GCM. Time averaging was performed over 400 Earth-days. The westerly equatorial jet has a width of about 30–45°.

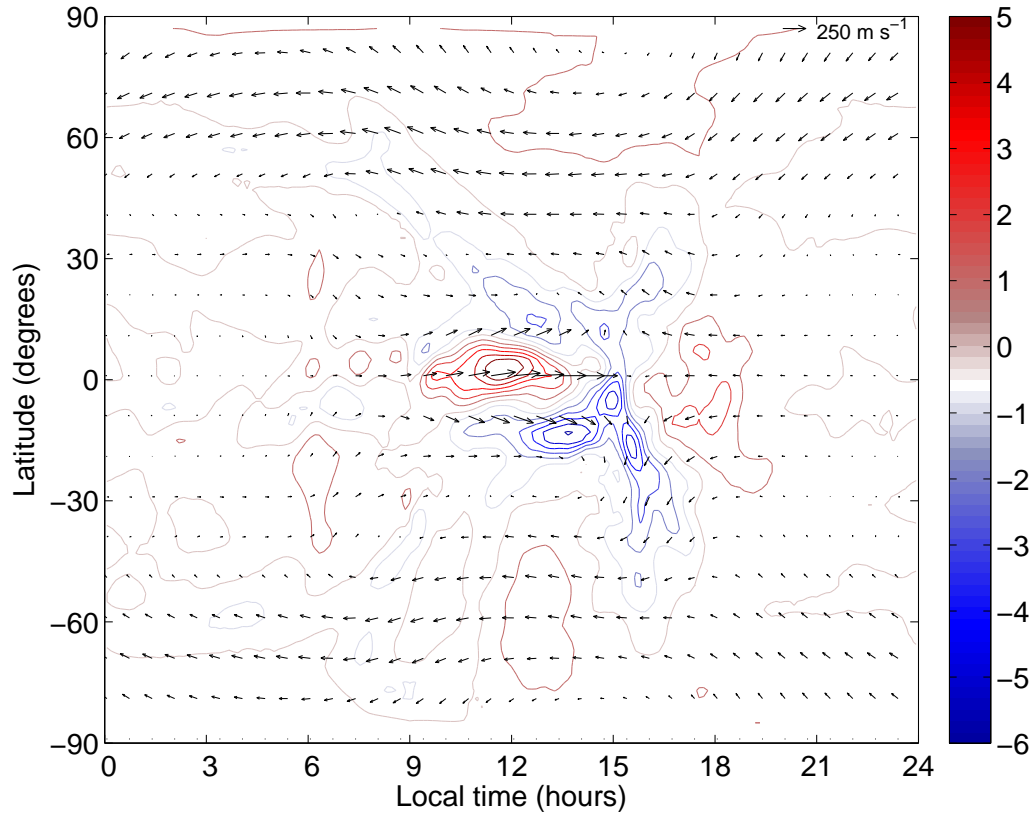


Figure 5: Horizontal winds (arrows, in  $\text{m s}^{-1}$ ) and vertical winds in pressure coordinates (colored contours, in  $10^{-2} \text{ Pa s}$ ) from simple GCM with global mean surface pressure= $10^5 \text{ Pa}$  and surface albedo=0.4 case. Time averaging was performed over 400 Earth-days. The winds are shown as an example case of the circulation in the boundary layer at 9377 Pa. Note that in pressure coordinates positive vertical wind is downward.

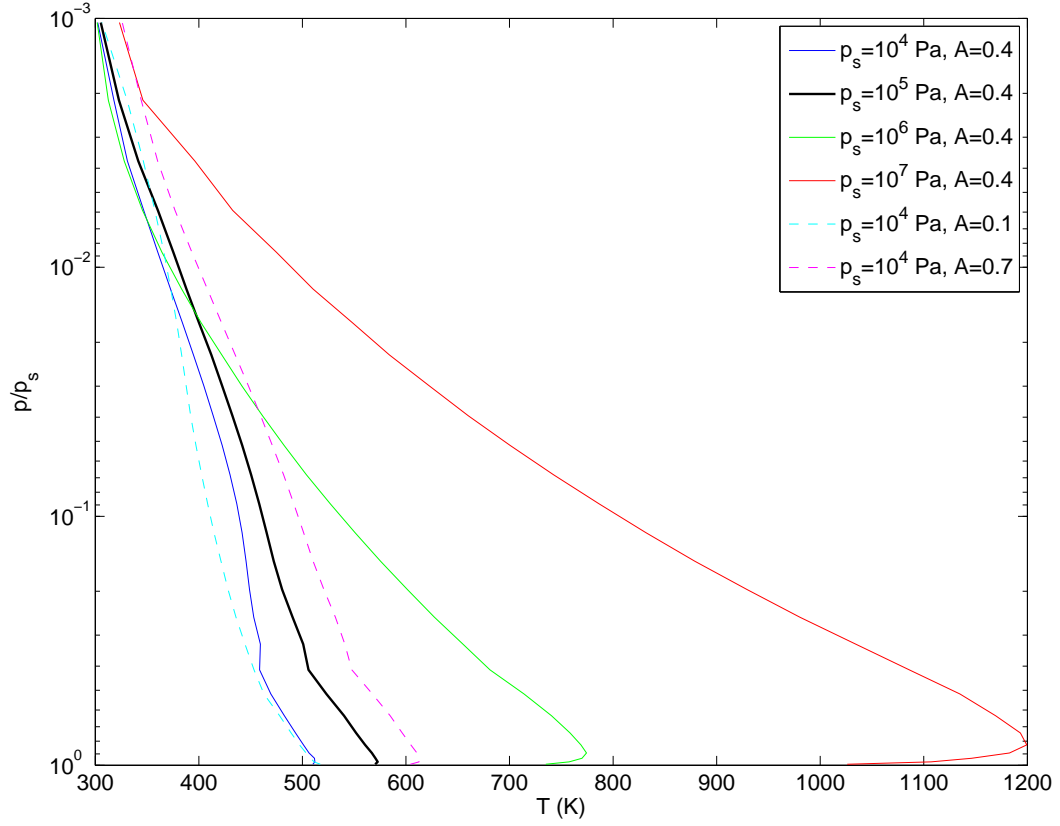


Figure 6: Temperature profiles from simple GCM as a function of global mean surface pressure and surface albedo. The profiles are time averaged over 400 Earth-days. All profiles are shown for the equator and 12 hours LT. The profiles are plotted as a function of  $\sigma$  level  $p/p_s$  such that all profiles could be displayed on the same plot.

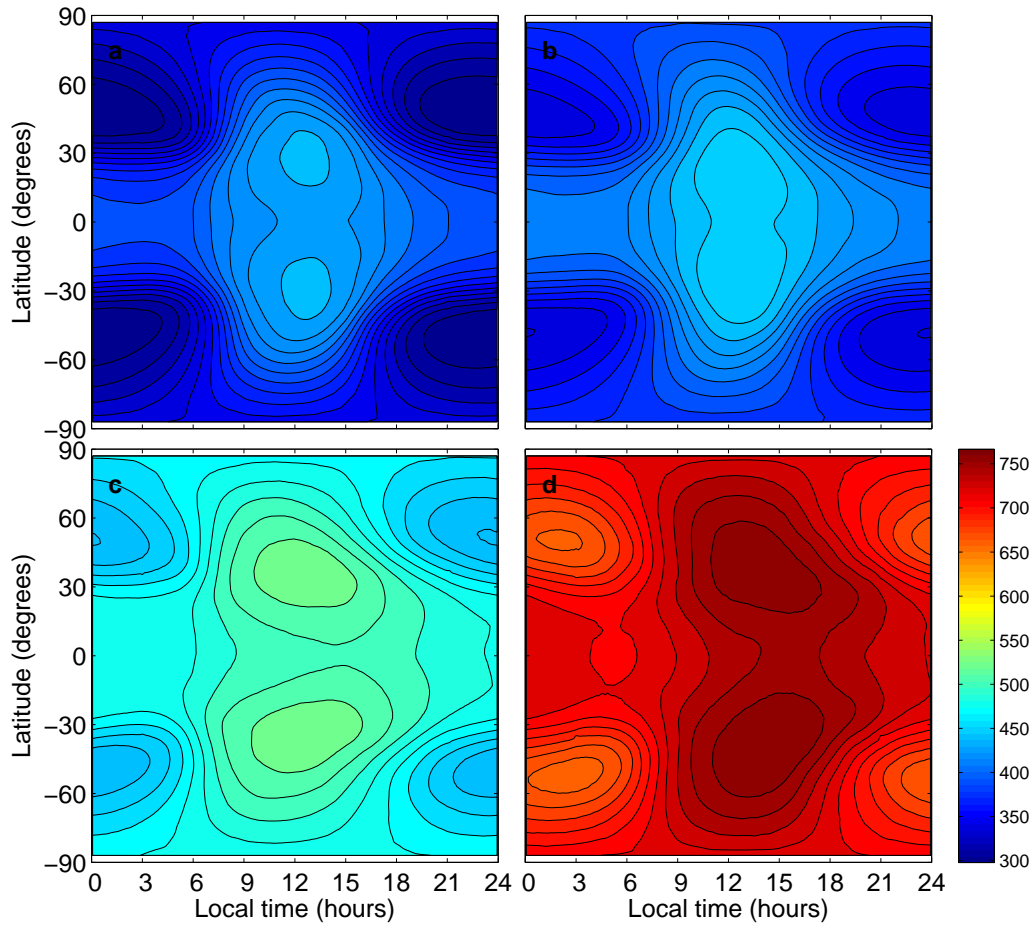


Figure 7: Simple GCM temperature as a function of global mean surface pressure: (a)  $p_s = 10^4$  Pa, (b)  $p_s = 10^5$  Pa, (c)  $p_s = 10^6$  Pa, and (d)  $p_s = 10^7$  Pa. All cases have  $A = 0.4$ , are time averaged over 400 Earth-days, and are shown at the same  $\sigma$  level  $p/p_s = 0.068$ .



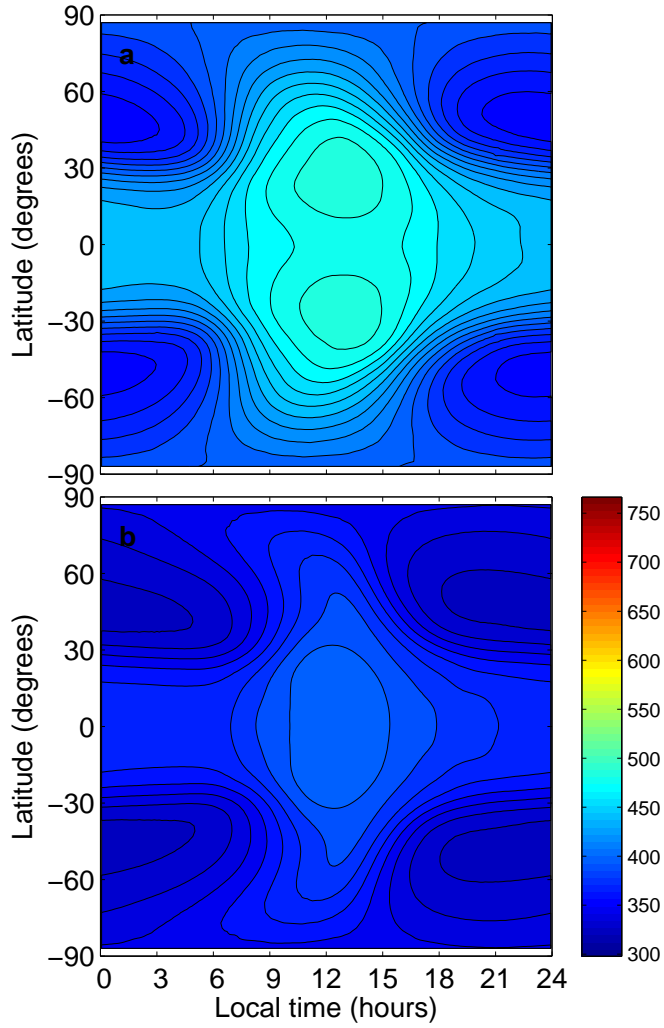


Figure 8: Simple GCM temperature as a function of surface albedo: (a)  $A = 0.1$ , (b)  $A = 0.7$  Pa. All cases have  $p_s = 10^5$  Pa, are time averaged over 400 Earth-days, and are shown at the same  $\sigma$  level  $p/p_s = 0.068$ . Taken with panel (b) of Fig. 7, these plots form a progression of surface albedos from 0.1–0.7.

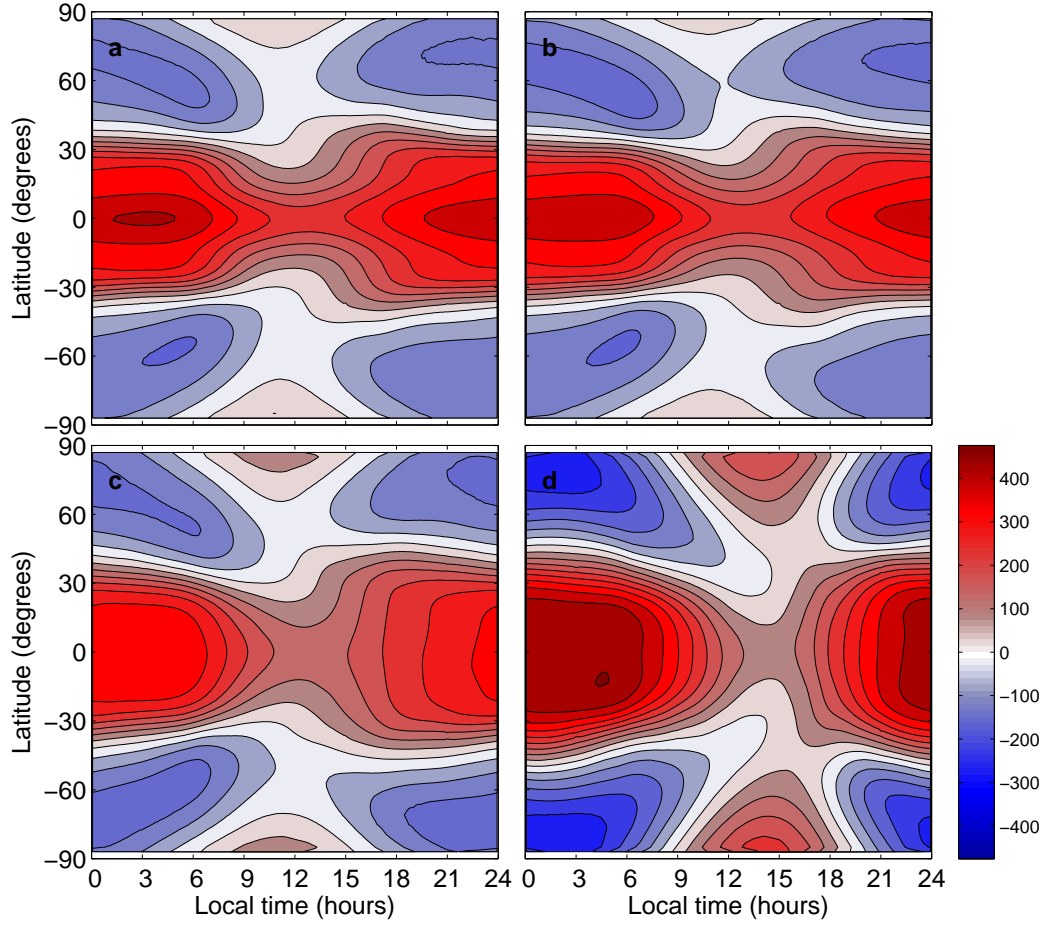


Figure 9: Simple GCM zonal winds as a function of global mean surface pressure: (a)  $p_s = 10^4$  Pa, (b)  $p_s = 10^5$  Pa, (c)  $p_s = 10^6$  Pa, and (d)  $p_s = 10^7$  Pa. All cases have  $A = 0.4$ , are time averaged over 400 Earth-days, and are shown at the same  $\sigma$  level  $p/p_s = 0.068$ . Positive corresponds to westerly flow.

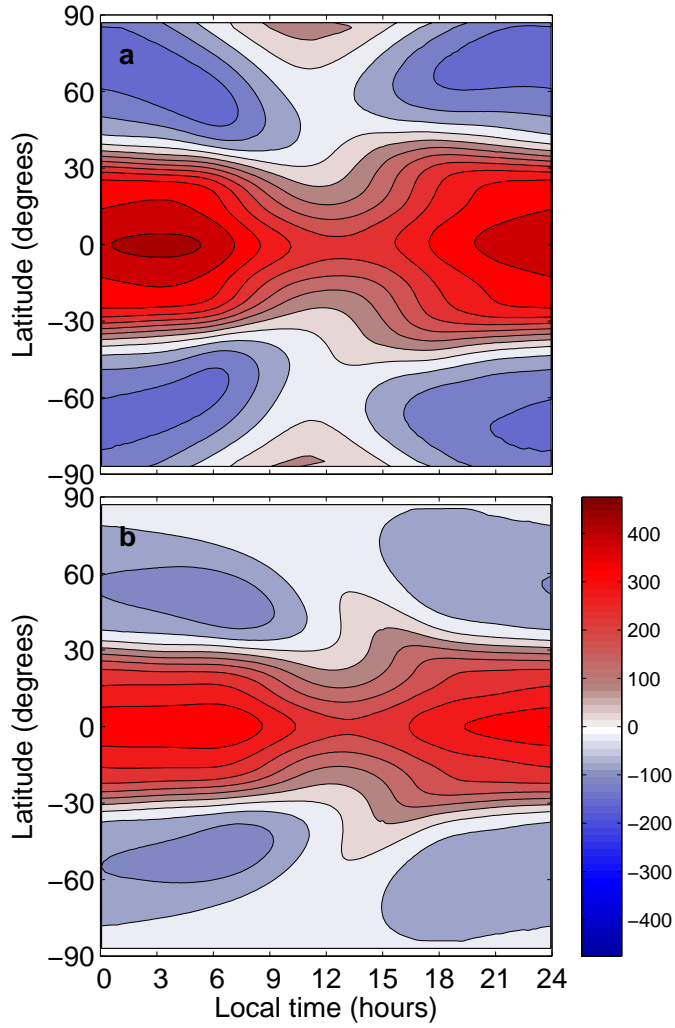


Figure 10: Simple GCM zonal winds as a function of surface albedo: (a)  $A = 0.1$ , (b)  $A = 0.7$  Pa. All cases have  $p_s = 10^5$  Pa, are time averaged over 400 Earth-days, and are shown at the same  $\sigma$  level  $p/p_s = 0.068$ . Taken with panel (b) of Fig. 9, these plots form a progression of surface albedos from 0.1–0.7. Positive corresponds to westerly flow.

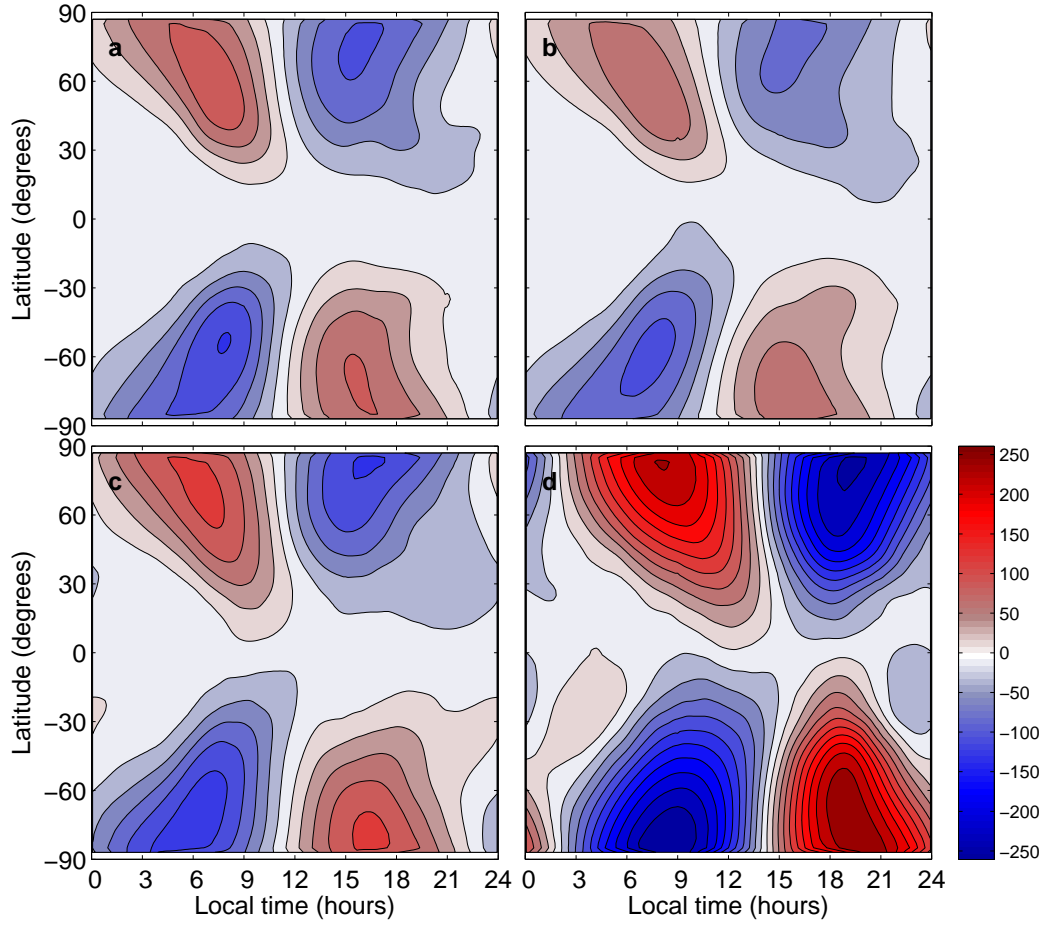


Figure 11: Simple GCM meridional winds as a function of global mean surface pressure: (a)  $p_s = 10^4$  Pa, (b)  $p_s = 10^5$  Pa, (c)  $p_s = 10^6$  Pa, and (d)  $p_s = 10^7$  Pa. All cases have  $A = 0.4$ , are time averaged over 400 Earth-days, and are shown at the same  $\sigma$  level  $p/p_s = 0.068$ . Positive corresponds to southerly flow.

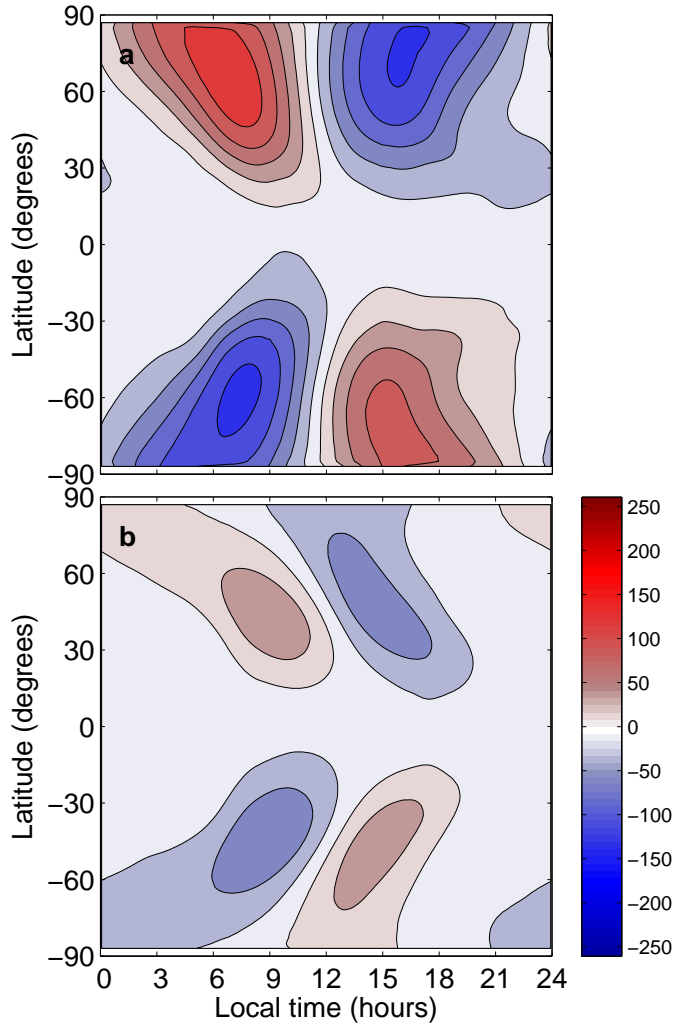


Figure 12: Simple GCM meridional winds as a function of surface albedo: (a)  $A = 0.1$ , (b)  $A = 0.7$  Pa. All cases have  $p_s = 10^5$  Pa, are time averaged over 400 Earth-days, and are shown at the same  $\sigma$  level  $p/p_s = 0.068$ . Taken with panel (b) of Fig. 11, these plots form a progression of surface albedos from 0.1–0.7. Positive corresponds to southerly flow.

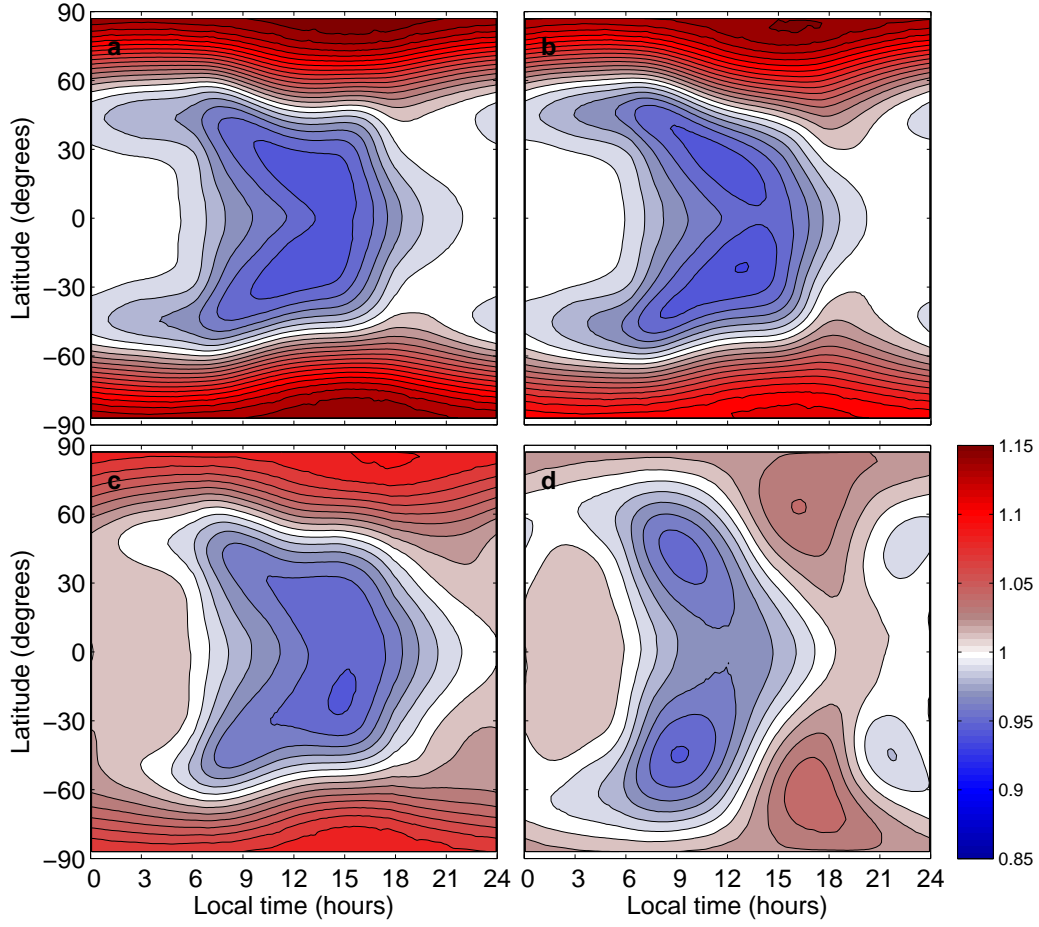


Figure 13: Simple GCM surface pressure variation as a function of global mean surface pressure: (a)  $p_s = 10^4$  Pa, (b)  $p_s = 10^5$  Pa, (c)  $p_s = 10^6$  Pa, and (d)  $p_s = 10^7$  Pa. Each panel is normalized by the global mean surface pressure for that case. All cases have  $A = 0.4$  and are time averaged over 400 Earth-days. Positive corresponds to southerly flow.

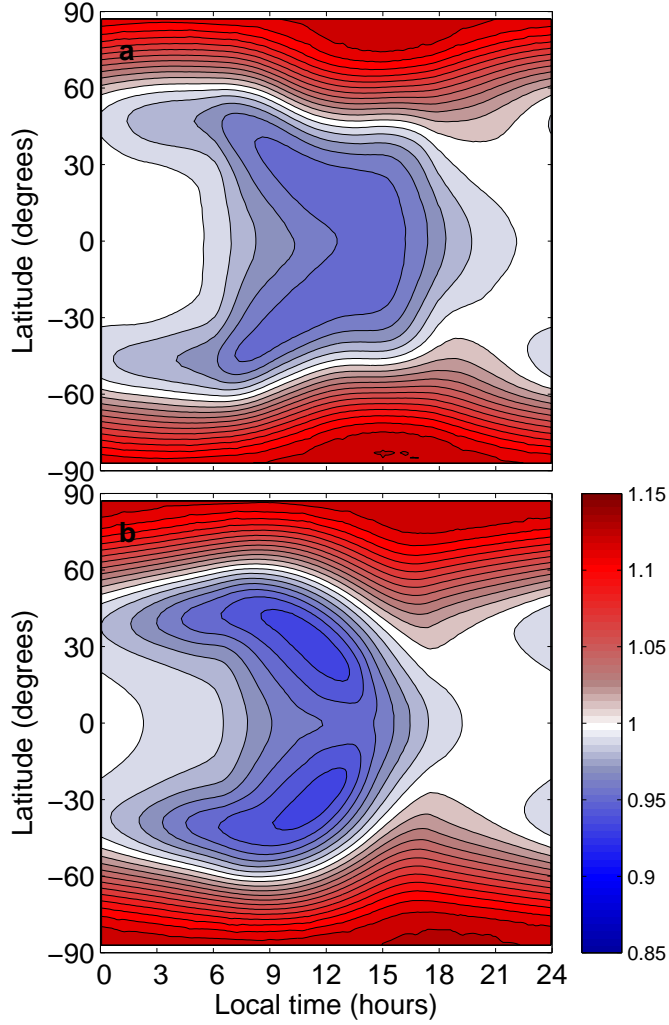


Figure 14: Simple GCM surface pressure variation as a function of surface albedo: (a)  $A = 0.1$ , (b)  $A = 0.7$  Pa. All cases have  $p_s = 10^5$  Pa and are time averaged over 400 Earth-days. Each panel is normalized by the global mean surface pressure for that case. Taken with panel (b) of Fig. 13, these plots form a progression of surface albedos from 0.1–0.7.

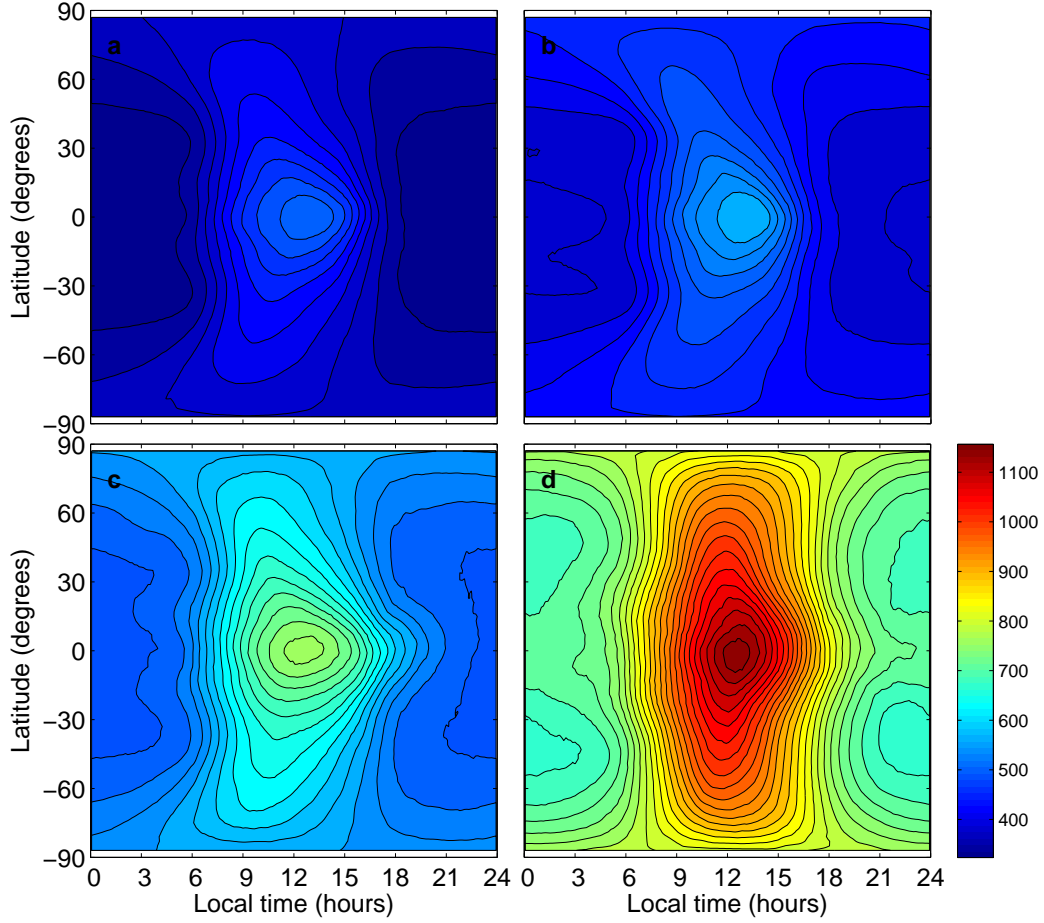


Figure 15: Simple GCM temperature as a function of global mean surface pressure: (a)  $p_s = 10^4$  Pa, (b)  $p_s = 10^5$  Pa, (c)  $p_s = 10^6$  Pa, and (d)  $p_s = 10^7$  Pa. All cases have  $A = 0.4$ , are time averaged over 400 Earth-days, and are shown at the same  $\sigma$  level  $p/p_s = 0.9377$ .



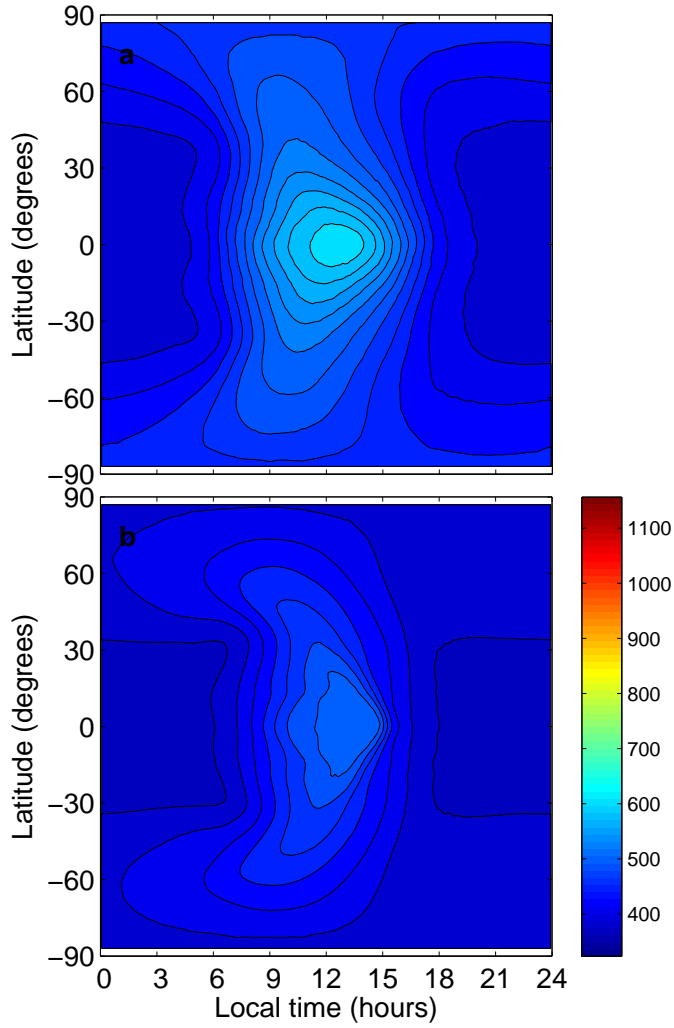


Figure 16: Simple GCM temperature as a function of surface albedo: (a)  $A = 0.1$ , (b)  $A = 0.7$  Pa. All cases have  $p_s = 10^5$  Pa, are time averaged over 400 Earth-days, and are shown at the same  $\sigma$  level  $p/p_s = 0.9377$ . Taken with panel (b) of Fig. 15, these plots form a progression of surface albedos from 0.1–0.7.

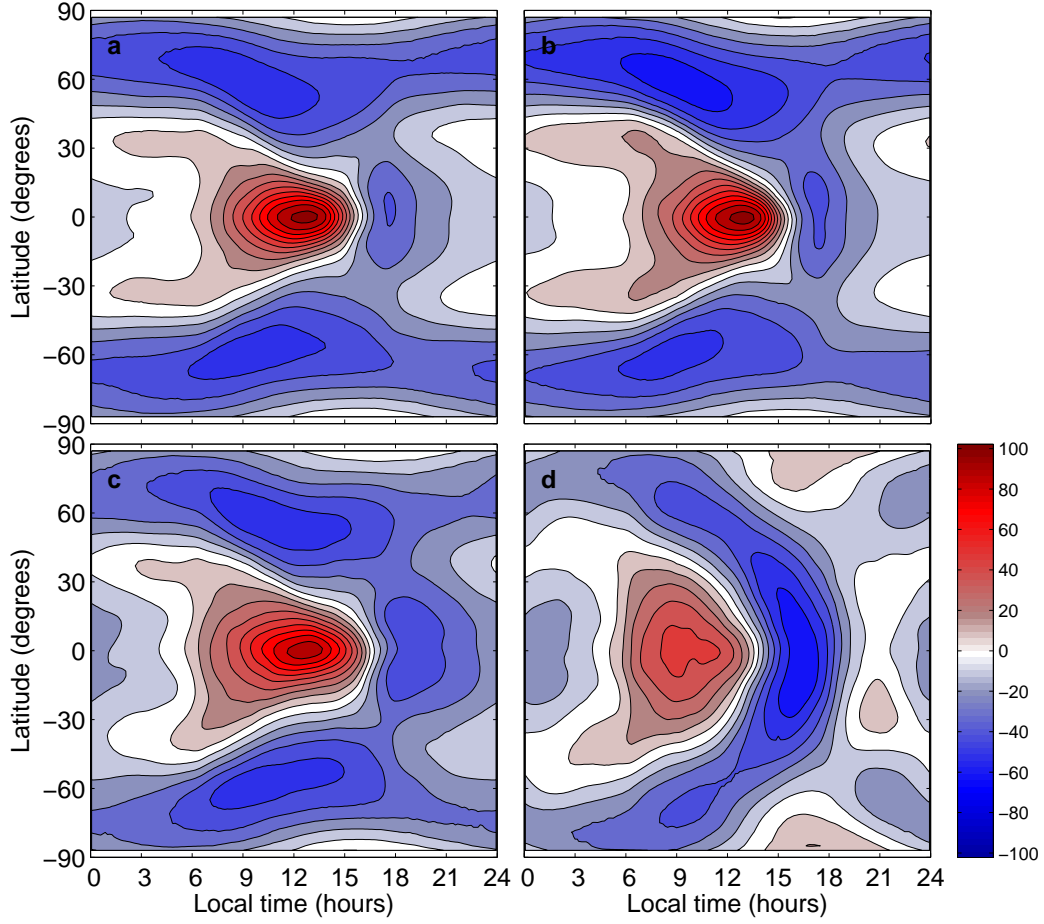


Figure 17: Simple GCM zonal winds as a function of global mean surface pressure: (a)  $p_s = 10^4$  Pa, (b)  $p_s = 10^5$  Pa, (c)  $p_s = 10^6$  Pa, and (d)  $p_s = 10^7$  Pa. All cases have  $A = 0.4$ , are time averaged over 400 Earth-days, and are shown at the same  $\sigma$  level  $p/p_s = 0.9377$ . Positive corresponds to westerly flow.

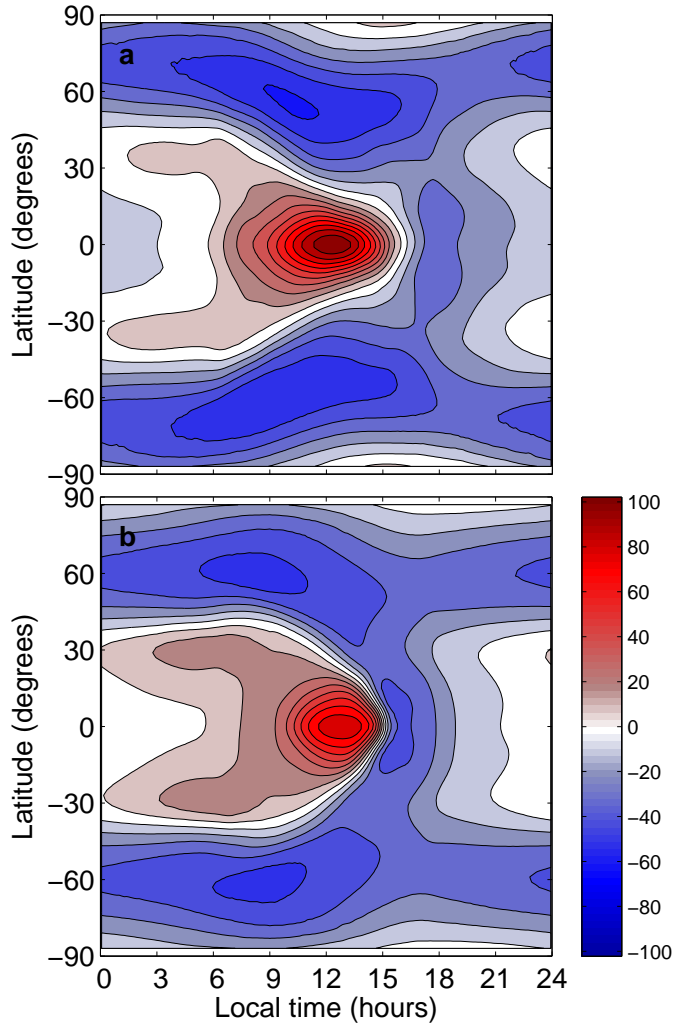


Figure 18: Simple GCM zonal winds as a function of surface albedo: (a)  $A = 0.1$ , (b)  $A = 0.7$  Pa. All cases have  $p_s = 10^5$  Pa, are time averaged over 400 Earth-days, and are shown at the same  $\sigma$  level  $p/p_s = 0.068$ . Taken with panel (b) of Fig. 17, these plots form a progression of surface albedos from 0.1–0.7. Positive corresponds to westerly flow.

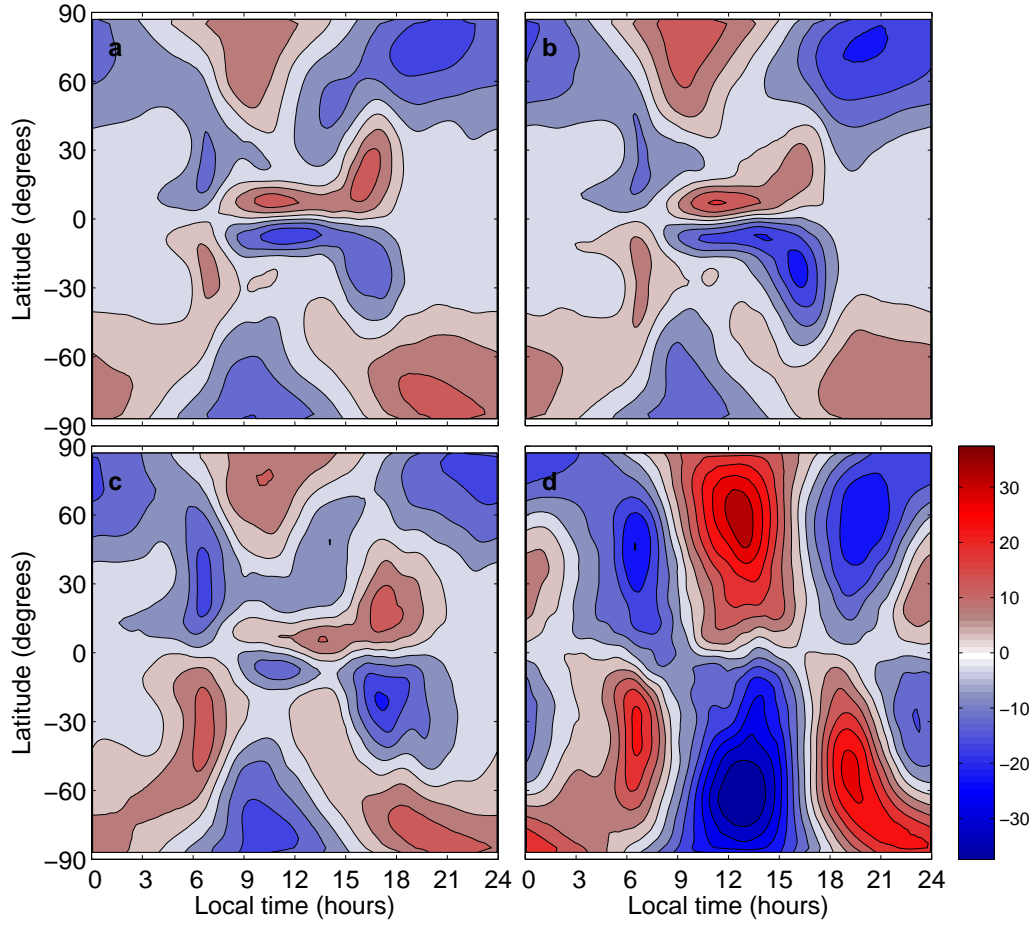


Figure 19: Simple GCM meridional winds as a function of global mean surface pressure: (a)  $p_s = 10^4$  Pa, (b)  $p_s = 10^5$  Pa, (c)  $p_s = 10^6$  Pa, and (d)  $p_s = 10^7$  Pa. All cases have  $A = 0.4$ , are time averaged over 400 Earth-days, and are shown at the same  $\sigma$  level  $p/p_s = 0.9377$ . Positive corresponds to southerly flow.

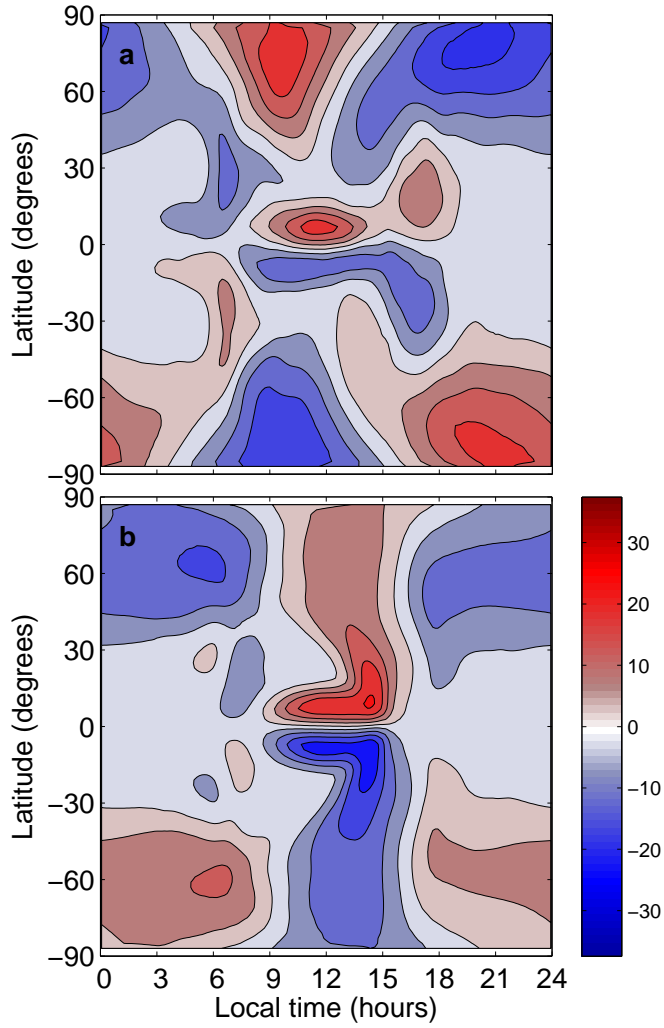


Figure 20: Simple GCM meridional winds as a function of surface albedo: (a)  $A = 0.1$ , (b)  $A = 0.7$  Pa. All cases have  $p_s = 10^5$  Pa, are time averaged over 400 Earth-days, and are shown at the same  $\sigma$  level  $p/p_s = 0.9377$ . Taken with panel (b) of Fig. 19, these plots form a progression of surface albedos from 0.1–0.7. Positive corresponds to southerly flow.

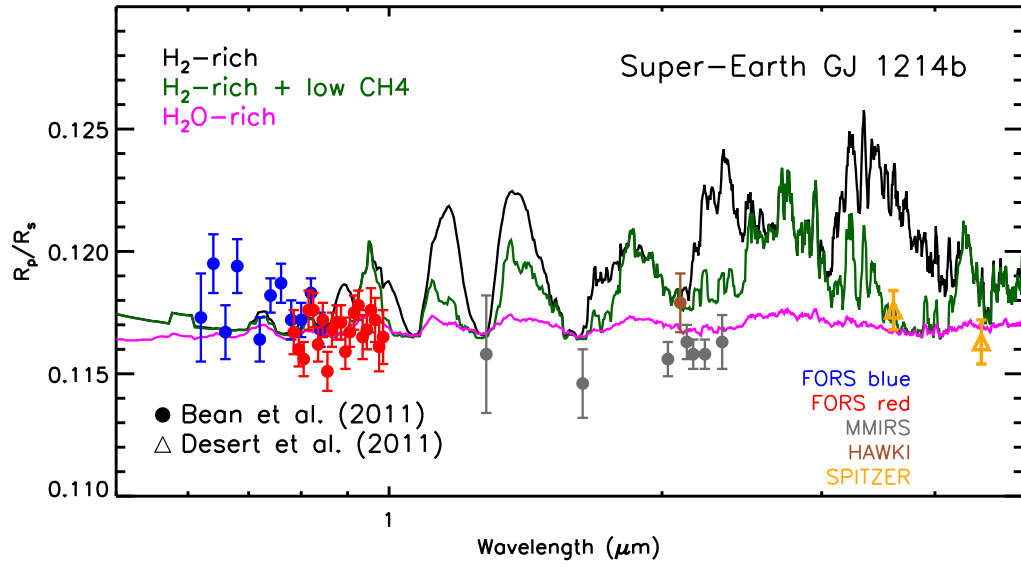


Figure 21: Comparison of model spectra calculated from simple GCM output. The  $10^5$  Pa global mean surface pressure and 0.4 surface albedo cases are shown with the composition indicated in the figure. The  $\text{H}_2\text{O}$  case is consistent with observations but the  $\text{H}_2$  cases are not.